

Multidimensional Small Baseline Subset (Msbas) Software for Constrained and Unconstrained Deformation Analysis of Partially Coherent Dinsar and Speckle Offset Data

Sergey V. Samsonov

To cite this article: Sergey V. Samsonov (2024) Multidimensional Small Baseline Subset (Msbas) Software for Constrained and Unconstrained Deformation Analysis of Partially Coherent Dinsar and Speckle Offset Data, Canadian Journal of Remote Sensing, 50:1, 2424753, DOI: [10.1080/07038992.2024.2424753](https://doi.org/10.1080/07038992.2024.2424753)

To link to this article: <https://doi.org/10.1080/07038992.2024.2424753>



© 2024 Natural Resources Canada,
Government of Canada. Published by
Informa UK Limited, trading as Taylor &
Francis Group



Published online: 15 Dec 2024.



Submit your article to this journal



Article views: 36



View related articles



View Crossmark data

Multidimensional Small Baseline Subset (Msbas) Software for Constrained and Unconstrained Deformation Analysis of Partially Coherent Dinsar and Speckle Offset Data

Logiciel de sous-ensemble multidimensionnelle à courte ligne de base (Multidimensional Small Baseline Subset [MSBAS]) pour l'analyse déformation contrainte et non contrainte des données partiellement cohérentes de DInSAR et les données de décalage des taches

Sergey V. Samsonov

Canada Centre for Mapping and Earth Observation, Natural Resources Canada, 580 Booth Street, Ottawa, ONK1A 0E4, Canada

ABSTRACT

Differential Interferometric Synthetic Aperture Radar (DInSAR) and speckle offset data are used to measure ground deformation. Computing deformation time series from these data can be challenging due to varying radar line-of-sight acquisition geometry, rapid coherence loss, and the large datasets involved requiring computationally intensive processing. The Multidimensional Small Baseline Subset (MSBAS) Software is designed to compute deformation time series from these data, and its parallelized version is optimized to handle large datasets from modern SAR satellites. The software can produce 1D, 2D, and 3D Surface-Parallel and Aspect-Parallel Flow constrained and 3D unconstrained or 4D deformation time series. It runs on workstations and clusters utilizing OpenMP and MPI/OpenMP. This study presents novel results demonstrating MSBAS capabilities, such as landslides in Northwest Territories, Argentina, and Colombia, as well as tectonic deformation and subsidence in Turkey and Yemen. A 4D deformation time series of glacier flow and surge at the Malaspina Glacier in Alaska is showcased. Equations for solving multidimensional problems are included along with processing parameters and supplemental data used to create constraints. The manuscript serves as a comprehensive manual for the MSBAS Software Version 10. The source code is available.

RÉSUMÉ

Des données radar à ouverture synthétique interférométrique différentielle ([DInSAR]) et les données de décalage des taches sont utilisées pour mesurer la déformation du sol. Des calculs des déformations en séries temporelles peuvent être difficiles en raison de la géométrie d'acquisition radar variable, de la perte rapide de cohérence et des grands ensembles de données impliqués nécessitant un traitement informatique intensif. Le logiciel sous-ensemble multidimensionnel à courte ligne de base (MSBAS) est conçu pour calculer des séries temporelles de déformation à partir de ces données, et sa version parallélisée est optimisée pour gérer de grands ensembles de données provenant de satellites SAR modernes. Le logiciel peut produire des séries temporelles 1D, 2D et 3D de déformation en surface-parallèle et en aspect-parallèle contraintes et 3D sans contrainte ou 4D. Il fonctionne sur des postes de travail et des clusters utilisant OpenMP et MPI/OpenMP. Cette étude présente des nouveaux résultats démontrant les capacités de MSBAS, tels que les glissements de terrain dans les Territoires du Nord-Ouest, en Argentine et en Colombie, ainsi que la déformation tectonique et l'affaissement en Turquie et au Yémen. Une série temporelle de déformations 4D du flux et de la montée des glaciers du glacier Malaspina en Alaska est présentée. Les équations pour résoudre des problèmes multidimensionnels sont incluses avec les paramètres de traitement et les données supplémentaires utilisées pour créer des contraintes. Le manuscrit sert de manuel complet pour la version 10 du logiciel MSBAS. Le code source est disponible.

ARTICLE HISTORY

Received 5 July 2024

Accepted 21 October 2024

1. Introduction

The Differential Interferometric Synthetic Aperture Radar (DInSAR) technique is a powerful tool for monitoring ground deformation caused by various natural and human activities (Massonnet and Feigl 1998; Rosen et al. 2000). It can provide measurements with meter and even sub-meter spatial resolution and sub-centimetre precision across large areas, making it an ideal method for detecting and tracking changes of the Earth's surface. The Speckle Offset tracking technique (SPO) also computes ground deformation at slightly lower precision, and is particularly suitable for measuring large deformation, for example, due to glacier flow (Strozzi et al. 2002).

The DInSAR/SPO processing can be divided into two steps. First, individual DInSAR/SPO products (interferograms and/or range/azimuth offset maps) are computed from SAR data, and then, if required, these products are used for computing deformation time series. This study focuses on the second step of computing deformation time series. Specifically, it describes the Multidimensional Small Baseline Subset (MSBAS) software developed by the author for computing deformation time series from repeatedly acquired DInSAR and/or SPO data. Depending on the input data and processing parameters, it can produce a 1D (line-of-sight, LOS), 2D (east and vertical), Aspect-Parallel Flow (APF) and Surface-Parallel Flow (SPF) constrained and unconstrained 3D (north, east, and vertical), and 4D (north, east, and two vertical subcomponents) deformation time series. Table 1 lists possible combinations

of input data, processing parameters, and the resulting dimensionality of the computed time series. For example, using four datasets, range and azimuth offsets obtained on ascending and descending passes (No 8 in Table 1), 3D time series can be produced.

Two versions of the MSBAS Software have been previously released. The MSBAS Software Version 3 could only compute 1D and 2D deformation time series from fully coherent data obtained on ascending and descending passes (Samsonov and d'Oreye 2017). It had additional functionality, such as the topographic correction, temporal and spatial filtering of the input and output data and the ability to extract time series for selected pixels interactively. MSBAS Software Version 6 could compute 1D–4D deformation time series from fully coherent data obtained on ascending and descending passes; however, it could only run on workstation-class devices; it used the Open Multi-Processing (OpenMP) Application Program Interface (API) for processing parallelization.

The processing algorithm of MSBAS Software Version 10 (subsequently referred to as MSBAS) is designed to compute deformation time series from partially coherent input data. The coefficient matrix is constructed and inverted individually for each pixel using the double precision Linear Algebra Package (LAPACK) *DGELSD* subroutine, which computes a minimum-norm solution to the real linear least-squares problem using Singular Value Decomposition (SVD). During inversion, before adding the regularization terms, a matrix rank for each pixel is computed and saved to a file; then in post processing, the computed

Table 1. Dimensionality of MSBAS time series as determined by type of input data and control flags.

No	MSBAS Technique	DInSAR / SPO – RO _{asc}	DInSAR / SPO – RO _{dsc}	SPO – AO _{asc}	SPO – AO _{dsc}	α_h	$\frac{\partial h}{\partial x_n}, \frac{\partial h}{\partial x_e}$	L_FLAG = 1,...,4
1	1D	×						
2	1D		×					
3	1D			×				
4	1D					×		
5	2D	×	×				×	
6	3D	×	×		×			
7	3D	×	×	×			×	
8	3D	×	×	×	×	×		
9	3DAPF	×	×					
10	3DSPF	×			×			
11	3DSPF			×		×		
12	3DSPF	×	×	×	×			
13	3DSPF	×	×			×		
14	3DSPF	×	×	×	×	×		
15	4D	×	×	×	×		×	
16	4D	×	×			×	×	×
17	4D	×	×	×	×	×	×	×

DInSAR / SPO – RO_{asc}, DInSAR / SPO – RO_{dsc}, SPO – AO_{asc}, SPO – AO_{dsc} are range and azimuth measurements obtained on ascending and descending passes.

DInSAR and SPO-RO range measurements are considered equivalent. More than one set of similar types can be used. α_h is elevation aspect angle measured in radians. $\frac{\partial h}{\partial x_n}$ and $\frac{\partial h}{\partial x_e}$ are elevation first derivatives along north and east directions. L_FLAG = 1,...,4 is processing control flag that enables 4D analysis. APF is Aspect-Parallel Flow constraint. SPF is Surface-Parallel Flow constraint.

Table 2. Studies that use MSBAS Software for computing deformation time series.

Application	Technique	Region	Study(ies)
Mining – Coal	2D	France/Germany and Alberta, Canada	(Samsonov et al. 2013a, 2024)
Mining – Potash	2D	Saskatchewan, Canada	(Samsonov et al. 2013b, Samsonov et al. 2014b, 2024)
Mining – Potash	1D, 2D	Perm Krai, Russia	(Samsonov and Baryakh 2020)
Mining – Oil	1D	Alberta, Canada	(Pearse et al. 2014; Samsonov 2017; Samsonov et al. 2024)
Subsidence	2D	Mexico City	(Samsonov and d'Oreye 2017)
Subsidence	2D	Seattle	(Samsonov et al. 2016b)
Subsidence	2D	Vancouver	(Samsonov et al. 2014a)
Cryosphere – Pingo	2D	NWT, Canada	(Samsonov et al. 2016c)
Cryosphere – Glaciers	3D	British Columbia, Canada	(Samsonov et al. 2021a)
Cryosphere – Glaciers	3DSPF	Nunavut, Canada	(Samsonov 2019)
Cryosphere – Glaciers	4D	British Columbia, Canada	(Samsonov et al. 2021b)
Cryosphere – Glaciers	4D	Alaska, USA	(Samsonov 2022)
Hazards-Landslides	3DSPF	Bukavu, DR Congo	(Dille et al. 2021, 2022; Samsonov et al. 2020)
Hazards-Landslides	1D, 2D	British Columbia, Canada	(Samsonov and Blais-Stevens 2023)
Hazards-Landslides	2D, 3DSPF, 3DAPF	Alberta/NWT, Canada	(Samsonov and Blais-Stevens 2024)
Hazards-Volcanoes	2D	various	(Camacho et al. 2020; Samsonov et al. 2014c, 2016a)
Hazards-Volcanoes	2D	(cont.)	(Derauw et al. 2020; Lundgren et al. 2020)
CO ₂ sequestration	2D	Saskatchewan, Canada	(Czarnogorska et al. 2016; Samsonov et al. 2015; Vasco et al. 2020a)
Geothermal power	2D	Baja California, Mexico	(Samsonov et al. 2017; Vasco et al. 2020b)
Natural gas storage	2D	California, USA	(Vasco et al. 2021)
Others	2D	various	(Samsonov et al. 2014d; Smittarello et al. 2022)

matrix rank can be used to mask out low-rank pixels. As the computation of SVD for each pixel of a large matrix is time-consuming, the MSBAS Software has been redesigned to optimally run on clusters by distributing an equal number of raster lines to different nodes using Message Passing Interface (MPI) API. Open MP API is employed to further distribute processing between cores on each node.

The MSBAS presented here has been optimized to process large datasets. As a result, it does not support some of the previous functionality, such as topographic correction and temporal and spatial filtering of input and output data. Topographic correction is no longer necessary because modern Digital Elevation Models (DEMs) have sufficiently high precision. The spatial filtering of input data and temporal and spatial filtering of output data can be performed outside of MSBAS using advanced time series and image processing techniques that are widely available (e.g., several libraries written in R language). The interactive extraction of time series for selected pixels from raster data is no longer supported because time series can be extracted in post-processing using the additional software *msbas_extract* which is also provided.

The MSBAS Software has been utilized in several studies (Table 2). The deformation processes can be divided into anthropogenic, slow natural and fast natural deformation. Studies of anthropogenic deformation due to mining activities, fluid (oil/gas/groundwater/CO₂) injection and extraction, and natural-slow deformation caused by volcanic and

tectonic sources use DInSAR data and MSBAS-1D and 2D techniques. The MSBAS-2D method assumes no significant deformation in the north direction, making the 2D solution an approximation. The MSBAS-3DAPF and 3DSPF techniques can be used for studying slow-moving deep-seated landslides. Lastly, studies of natural-fast deformation caused by glacier flow use DInSAR and/or SPO data and MSBAS-3D, 3DAPF, 3DSPF, and 4D techniques. Currently, the MSBAS Software is part of three operational automatic processing systems (Dudley and Samsonov 2020, 2021; d'Oreye et al. 2021).

This study's aim is to demonstrate the new functionality of the MSBAS Software through examples. Six examples reveal new findings, while one example, in the Northwest Territories of Canada, has been previously described (Samsonov and Blais-Stevens 2024). The complete theoretical framework for the technique can be found in previous studies, specifically Samsonov and d'Oreye (2012, 2017); Samsonov et al. (2021a) but the key reference equations are presented in the following sections for completeness.

The MSBAS Software is available from Samsonov (2024).

2. Methodology

Using SAR data acquired repeatedly over a study area, DInSAR measures ground deformation in the range direction ρ^r , which is equal to the projection of the deformation (or displacement) vector on the satellite line-of-sight. Thus, DInSAR measurements contain

contributions of north d_n , east d_e , and vertical d_u deformation components. DInSAR processing requires phase unwrapping, which can be accurately performed only in the case of small to moderate deformation. The Speckle Offset tracking technique (SPO) also measures ground deformation in the range direction ρ^r , called range offsets (SPO-RO), and deformation along the satellite heading (also called flight direction or azimuth) ρ^a , called azimuth offsets (SPO-AO). As the computation of range and azimuth offsets does not require phase unwrapping the SPO technique is suitable for measuring large ground deformation, such as that caused by glacier flow. The precision of range and azimuth offsets depends on the spatial resolution of SAR data and is usually lower than the precision of DInSAR. MSBAS framework does not distinguish DInSAR and SPO-RO; both are abbreviated ρ^r . In MSBAS processing, DInSAR data can be substituted for SPO-RO data, or both datasets can be used simultaneously.

[Equations \(1\)–\(3\)](#) (Samsonov and d'Oreye 2012) provide the relationship between unknown north d_n , east d_e , and vertical d_u deformation components and observed DInSAR/SPO-RO ρ^r and SPO-AO ρ^a

$$\begin{aligned}\rho^r &= d_n s_n^r + d_e s_e^r + d_u s_u^r \\ \rho^a &= d_n s_n^a + d_e s_e^a + d_u s_u^a\end{aligned}\quad (1)$$

$s^r = (s_n^r, s_e^r, s_u^r)$ and $s^a = (s_n^a, s_e^a, s_u^a = 0)$ are the directional cosines along the range and azimuth directions that can be described in terms of satellite azimuth ϕ and SAR incidence angle θ

$$\begin{aligned}s^r &= (\sin \theta \sin \phi, -\sin \theta \cos \phi, \cos \theta) \\ s^a &= (\cos \phi, d_e \sin \phi, 0)\end{aligned}\quad (2)$$

or in terms of satellite orientation angle Φ and elevation angle Θ

$$\begin{aligned}s^r &= (\cos \Theta \sin \Phi, \cos \Theta \cos \Phi, \sin \Theta) \\ s^a &= (-\cos \Phi, \sin \Phi, 0).\end{aligned}\quad (3)$$

The satellite azimuth angle ϕ is measured clockwise between the direction of True North and the satellite flight direction projected on the Earth's surface. The SAR incidence angle θ is measured between the look vector pointing from the satellite to the surface of the Earth and the vertical downward direction. Its value is positive for the right-looking radar and negative for the left-looking radar. In the

mid-latitudes of Canada, the Sentinel-1 satellite azimuth angle on ascending passes is approximately 349° and on descending passes is approximately 193° , with a typically-used SAR incidence angle of 39° . These values found in metadata can be considered constant for the entire image only as a first-order approximation.

The elevation angle Θ is measured between the surface of the Earth and the look vector pointing to the satellite. The orientation angle Φ is measured counter clockwise between the east and the satellite flight direction projected on the Earth's surface. These values can be computed for each image pixel using a component of DInSAR processing software, such as *look_vector* in GAMMA software (Wegmüller et al. 2016).

The components of the deformation vector are positive in north, east and upward directions. The cumulative range, azimuth, north, east or vertical deformation time series $d(t)$ can be written as $d(t_0)=0$, $d(t_1)=d(t_0)+v_1 \Delta t_1$, or in general

$$d_i = \sum_{j=1}^i v_j \Delta t_j, \quad (4)$$

where $d_i = d(t_i)$ is the cumulative deformation at time t_i and $v_i = v(t_i)$ is the velocity during the time interval $\Delta t_i = t_i - t_{i-1}$. By default, in [Equation \(4\)](#) t_i are equal to the time of SAR acquisitions (in decimal year format). However, time can also be sampled at different regular or irregular intervals. For example, if t_i are regularly sampled once or twice annually, then v_i are the annual or semi annual deformation rates. If two t_i correspond to the time of the first and last SAR acquisitions, then v_{i-1} is the average deformation rate. Reducing the temporal resolution of the deformation time series can improve spatial coverage, shorten processing time, and make seasonal signals more evident.

Note that, in all the equations, the position of the bottom and top indices is chosen arbitrarily to make the equation appear compact. For example, the first ascending interferogram (or range offset) can be abbreviated as $\rho_1^{r,asc}$ or $\rho_{r,l,asc}$

2.1. MSBAS-1D

Assume for simplicity that three SAR images were acquired on ascending passes at t_0 , t_1 , and t_2 and two interferograms $\rho_1^{r,asc}$ and $\rho_2^{r,asc}$ were computed. Then, the MSBAS-1D problem can be written for each image pixel as

$$\begin{bmatrix} \Delta t_1 & 0 \\ 0 & \Delta t_2 \end{bmatrix} \begin{bmatrix} v_1^{r,asc} \\ v_2^{r,asc} \end{bmatrix} = \begin{bmatrix} \rho_1^{r,asc} \\ \rho_2^{r,asc} \end{bmatrix}. \quad (5)$$

Equation (5) can be written in a matrix form as $Av=\rho$ and a solution of the problem as $v=A^{-1}\rho$. Thus, finding the solution of the MSBAS-1D problem is reduced to finding A^{-1} , the inverse of the matrix A , comprised of the time intervals Δt_p by applying SVD and then reconstructing cumulative deformation time series using Equation (4). Note that in glaciology, instead of cumulative deformation time series d_p , velocity v_i (or flow rate) time series is used. The 1D problems of computing deformation time series from either range or azimuth offsets are identical to Equation (5).

For smoothing the solution, regularization terms can be added to A and ρ , as explicitly demonstrated in Samsonov and d'Oreye (2017).

2.2. MSBAS-2D

If, in addition to data obtained on the ascending passes described above, data were also obtained on descending passes at approximately the same times, and two descending interferograms were generated, then the MSBAS-2D problem can be written as

$$\begin{bmatrix} s_e^{r,asc} \Delta t_1 & s_u^{r,asc} \Delta t_1 & 0 & 0 \\ 0 & 0 & s_e^{r,asc} \Delta t_2 & s_u^{r,asc} \Delta t_2 \\ s_e^{r,dsc} \Delta t_1 & s_u^{r,dsc} \Delta t_1 & 0 & 0 \\ 0 & 0 & s_e^{r,dsc} \Delta t_2 & s_u^{r,dsc} \Delta t_2 \end{bmatrix} \begin{bmatrix} v_1^e \\ v_1^u \\ v_2^e \\ v_2^u \end{bmatrix} = \begin{bmatrix} \rho_1^{r,asc} \\ \rho_2^{r,asc} \\ \rho_1^{r,dsc} \\ \rho_2^{r,dsc} \end{bmatrix}. \quad (6)$$

Thus, finding the solution of the MSBAS-2D problem (and other problems discussed below) is again reduced to finding the inverse A^{-1} of the matrix A , comprised of the time intervals Δt_i and the east and vertical components of the ascending $s^{r,asc}$ and descending $s^{r,dsc}$ look vectors. Since data on ascending and descending passes are typically acquired at different times, the problem is usually underdetermined. However, matrix A can still be constructed similarly, incorporating regularization terms, as explicitly demonstrated in Samsonov and d'Oreye (2017).

Note that if azimuth offset data ρ^a acquired on both ascending and descending passes are available, the 2D problem can be reformulated in terms of v^u and v^e . However, it is uncommon to have azimuth offsets ρ^a data without range offsets ρ^r data. Therefore, the MSBAS Software does not support this 2D scenario, even though it is theoretically possible.

2.3. MSBAS-3D(v1)

If, in addition to data obtained on ascending and descending passes ρ^r (either DInSAR or SPO-RO) described above, other ρ^r data acquired on a different pass and abbreviated here $[ad]sc$ are available, then the MSBAS-3D problem can be written as

$$\begin{bmatrix} s_n^{r,asc} \Delta t_1 & s_e^{r,asc} \Delta t_1 & s_u^{r,asc} \Delta t_1 & 0 & 0 & 0 \\ 0 & 0 & 0 & s_n^{r,asc} \Delta t_2 & s_e^{r,asc} \Delta t_2 & s_u^{r,asc} \Delta t_2 \\ s_n^{r,dsc} \Delta t_1 & s_e^{r,dsc} \Delta t_1 & s_u^{r,dsc} \Delta t_1 & 0 & 0 & 0 \\ 0 & 0 & 0 & s_n^{r,dsc} \Delta t_2 & s_e^{r,dsc} \Delta t_2 & s_u^{r,dsc} \Delta t_2 \\ s_n^{r,[ad]sc} \Delta t_1 & s_e^{r,[ad]sc} \Delta t_1 & s_u^{r,[ad]sc} \Delta t_1 & 0 & 0 & 0 \\ 0 & 0 & 0 & s_n^{r,[ad]sc} \Delta t_2 & s_e^{r,[ad]sc} \Delta t_2 & s_u^{r,[ad]sc} \Delta t_2 \end{bmatrix} \begin{bmatrix} v_1^n \\ v_1^e \\ v_1^u \\ v_2^n \\ v_2^e \\ v_2^u \end{bmatrix} = \begin{bmatrix} \rho_1^{r,asc} \\ \rho_2^{r,asc} \\ \rho_1^{r,dsc} \\ \rho_2^{r,dsc} \\ \rho_1^{r,[ad]sc} \\ \rho_2^{r,[ad]sc} \end{bmatrix}. \quad (7)$$

The abbreviation $[ad]sc$ utilizes a Linux wildcard (i.e., $[]$) so that one of the letters 'a' or 'd' can be selected at a time (i.e., data acquired on ascending asc or descending dsc passes). It is written in this way because it is also possible to have the airborne SAR data acquired on a pass that is neither ascending nor descending.

Thus, while $[ad]sc$ data can be acquired on either ascending, descending or other possible passes, for the solution to exist, the rank of a matrix

$$\begin{bmatrix} s_n^{r,asc} & s_e^{r,asc} & s_u^{r,asc} \\ s_n^{r,dsc} & s_e^{r,dsc} & s_u^{r,dsc} \\ s_n^{r,[ad]sc} & s_e^{r,[ad]sc} & s_u^{r,[ad]sc} \end{bmatrix} \quad (8)$$

must be equal to three, and the conditioning number, equal to the fraction of the largest and smallest singular values, should be small. Since such data are not readily available, this technique has not been tested in detail.

2.4. MSBAS-3D(v2)

If in addition to data obtained on ascending and descending passes ρ^r (either DInSAR or SPO-RO) described above, SPO-AO ρ^a are also available, then the MSBAS-3D problem can be written as

$$\begin{bmatrix} s_n^{r,asc} \Delta t_1 & s_e^{r,asc} \Delta t_1 & s_u^{r,asc} \Delta t_1 & 0 & 0 & 0 \\ 0 & 0 & 0 & s_n^{r,asc} \Delta t_2 & s_e^{r,asc} \Delta t_2 & s_u^{r,asc} \Delta t_2 \\ s_n^{r,dsc} \Delta t_1 & s_e^{r,dsc} \Delta t_1 & s_u^{r,dsc} \Delta t_1 & 0 & 0 & 0 \\ 0 & 0 & 0 & s_n^{r,dsc} \Delta t_2 & s_e^{r,dsc} \Delta t_2 & s_u^{r,dsc} \Delta t_2 \\ s_n^{a,asc} \Delta t_1 & s_e^{a,asc} \Delta t_1 & 0 & 0 & 0 & 0 \\ 0 & 0 & 0 & s_n^{a,asc} \Delta t_2 & s_e^{a,asc} \Delta t_2 & 0 \\ s_n^{a,dsc} \Delta t_1 & s_e^{a,dsc} \Delta t_1 & 0 & 0 & 0 & 0 \\ 0 & 0 & 0 & s_n^{a,dsc} \Delta t_2 & s_e^{a,dsc} \Delta t_2 & 0 \end{bmatrix} \begin{bmatrix} v_1^n \\ v_1^e \\ v_1^u \\ v_2^n \\ v_2^e \\ v_2^u \end{bmatrix} = \begin{bmatrix} \rho_1^{r,asc} \\ \rho_2^{r,asc} \\ \rho_1^{r,dsc} \\ \rho_2^{r,dsc} \\ \rho_1^{a,asc} \\ \rho_2^{a,asc} \\ \rho_1^{a,dsc} \\ \rho_2^{a,dsc} \end{bmatrix}. \quad (9)$$

It is uncommon to obtain ρ^a data for slow deformation due to its relatively low precision. Therefore, the MSBAS-3D problem only arises in glaciological applications where the deformation rate (flow velocity) is large. In the case of slow deformation, two constrained 3D problems can be formulated instead.

2.5. MSBAS-3DAPF

If data ρ^r obtained on both ascending and descending passes are available, and the motion is constrained to Aspect-Parallel Flow (APF), then the MSBAS-3DAPF problem can be written as

$$\begin{bmatrix} s_n^{r,asc} \Delta t_1 & s_e^{r,asc} \Delta t_1 & s_u^{r,asc} \Delta t_1 & 0 & 0 & 0 \\ 0 & 0 & 0 & s_n^{r,asc} \Delta t_2 & s_e^{r,asc} \Delta t_2 & s_u^{r,asc} \Delta t_2 \\ s_n^{r,dsc} \Delta t_1 & s_e^{r,dsc} \Delta t_1 & s_u^{r,dsc} \Delta t_1 & 0 & 0 & 0 \\ 0 & 0 & 0 & s_n^{r,dsc} \Delta t_2 & s_e^{r,dsc} \Delta t_2 & s_u^{r,dsc} \Delta t_2 \\ \sin \alpha_h & -\cos \alpha_h & 0 & 0 & 0 & 0 \\ 0 & 0 & 0 & \sin \alpha_h & -\cos \alpha_h & 0 \end{bmatrix} \begin{bmatrix} v_1^n \\ v_1^e \\ v_1^u \\ v_2^n \\ v_2^e \\ v_2^u \end{bmatrix} = \begin{bmatrix} \rho_1^{r,asc} \\ \rho_2^{r,asc} \\ \rho_1^{r,dsc} \\ \rho_2^{r,dsc} \\ 0 \\ 0 \end{bmatrix}. \quad (10)$$

This problem describes deformation in the direction of the aspect angle of the digital elevation model (DEM). The aspect angle is the angle between the line that runs along the steepest slope of the plane and the north direction. If the aspect angle α_h is computed from the north clockwise, then the constraint is $v^n \sin \alpha_h - v^e \cos \alpha_h = 0$. If the aspect angle is computed from the east counter clockwise, the constraint is $-v^n \cos \alpha_h + v^e \sin \alpha_h = 0$. Before computing the aspect angle, the DEM is typically low-pass filtered to produce a smoothed version.

2.6. MSBAS-3DSPF(v1)

If data obtained on both ascending and descending passes ρ^r (either DInSAR or SPO-RO) are available, and the motion is constrained to Surface-Parallel Flow (SPF), then the MSBAS-3DSPF problem can be written as

$$\begin{bmatrix} s_n^{r,asc} \Delta t_1 & s_e^{r,asc} \Delta t_1 & s_u^{r,asc} \Delta t_1 & 0 & 0 & 0 \\ 0 & 0 & 0 & s_n^{r,asc} \Delta t_2 & s_e^{r,asc} \Delta t_2 & s_u^{r,asc} \Delta t_2 \\ s_n^{r,dsc} \Delta t_1 & s_e^{r,dsc} \Delta t_1 & s_u^{r,dsc} \Delta t_1 & 0 & 0 & 0 \\ 0 & 0 & 0 & s_n^{r,dsc} \Delta t_2 & s_e^{r,dsc} \Delta t_2 & s_u^{r,dsc} \Delta t_2 \\ \frac{\partial h}{\partial x_n} & \frac{\partial h}{\partial x_n} & -1 & 0 & 0 & 0 \\ 0 & 0 & 0 & \frac{\partial h}{\partial x_n} & \frac{\partial h}{\partial x_n} & -1 \end{bmatrix} \begin{bmatrix} v_1^n \\ v_1^e \\ v_1^u \\ v_2^n \\ v_2^e \\ v_2^u \end{bmatrix} = \begin{bmatrix} \rho_1^{r,asc} \\ \rho_2^{r,asc} \\ \rho_1^{r,dsc} \\ \rho_2^{r,dsc} \\ 0 \\ 0 \end{bmatrix}. \quad (11)$$

This problem assumes that slow-moving deep-seated landslides slide along a buried surface that is roughly parallel to the smoothed surface topography. The combination of first derivatives along the north $\frac{\partial h}{\partial x_n}$ and east $\frac{\partial h}{\partial x_e}$ directions, where h is the value of elevation at the pixel, describe the SPF constraint $v^n \frac{\partial h}{\partial x_n} + v^e \frac{\partial h}{\partial x_e} = 0$. Similar to the previous example, the DEM is usually low-pass filtered to produce a smoothed version before computing the derivatives.

2.7. MSBAS-3DSPF(v2)

If azimuth offsets ρ^a are added to the 3DSPF problem described above, then the resulting problem is still of the 3DSPF type, and the motion remains constrained to the Surface-Parallel Flow.

$$\begin{bmatrix} s_n^{r,asc} \Delta t_1 & s_e^{r,asc} \Delta t_1 & s_u^{r,asc} \Delta t_1 & 0 & 0 & 0 \\ 0 & 0 & 0 & s_n^{r,asc} \Delta t_2 & s_e^{r,asc} \Delta t_2 & s_u^{r,asc} \Delta t_2 \\ s_n^{r,dsc} \Delta t_1 & s_e^{r,dsc} \Delta t_1 & s_u^{r,dsc} \Delta t_1 & 0 & 0 & 0 \\ 0 & 0 & 0 & s_n^{r,dsc} \Delta t_2 & s_e^{r,dsc} \Delta t_2 & s_u^{r,dsc} \Delta t_2 \\ s_n^{a,asc} \Delta t_1 & s_e^{a,asc} \Delta t_1 & 0 & 0 & 0 & 0 \\ 0 & 0 & 0 & s_n^{a,asc} \Delta t_2 & s_e^{a,asc} \Delta t_2 & 0 \\ s_n^{a,dsc} \Delta t_1 & s_e^{a,dsc} \Delta t_1 & 0 & 0 & 0 & 0 \\ 0 & 0 & 0 & s_n^{a,dsc} \Delta t_2 & s_e^{a,dsc} \Delta t_2 & 0 \\ \frac{\partial h}{\partial x_n} & \frac{\partial h}{\partial x_n} & -1 & 0 & 0 & 0 \\ 0 & 0 & 0 & \frac{\partial h}{\partial x_n} & \frac{\partial h}{\partial x_n} & -1 \end{bmatrix} \begin{bmatrix} v_1^n \\ v_1^e \\ v_1^u \\ v_2^n \\ v_2^e \\ v_2^u \end{bmatrix} = \begin{bmatrix} \rho_1^{r,asc} \\ \rho_2^{r,asc} \\ \rho_1^{r,dsc} \\ \rho_2^{r,dsc} \\ \rho_1^{a,asc} \\ \rho_2^{a,asc} \\ \rho_1^{a,dsc} \\ \rho_2^{a,dsc} \\ 0 \\ 0 \end{bmatrix}. \quad (12)$$

Adding the SPF constraint to the MSBAS-3D problem (or alternatively adding azimuth offsets to the MSBAS-3DSPF problem) makes the problem less general (i.e., of 3DSPF type) and, therefore, is not recommended.

2.8. MSBAS-4D

Finally, if the vertical deformation is subdivided into SPF v^{u1} and non-SPF v^{u2} components, the resulting MSBAS-4D problem can be written as

$$\begin{bmatrix}
 s_n^{r,asc} \Delta t_1 & s_e^{r,asc} \Delta t_1 & s_u^{r,asc} \Delta t_1 & s_u^{r,asc} \Delta t_1 & 0 & 0 & 0 & 0 \\
 0 & 0 & 0 & 0 & s_n^{r,asc} \Delta t_2 & s_e^{r,asc} \Delta t_2 & s_u^{r,asc} \Delta t_2 & s_u^{r,asc} \Delta t_2 \\
 s_n^{r,dsc} \Delta t_1 & s_e^{r,dsc} \Delta t_1 & s_u^{r,dsc} \Delta t_1 & s_u^{r,dsc} \Delta t_1 & 0 & 0 & 0 & 0 \\
 0 & 0 & 0 & 0 & s_n^{r,dsc} \Delta t_2 & s_e^{r,dsc} \Delta t_2 & s_u^{r,dsc} \Delta t_2 & s_u^{r,dsc} \Delta t_2 \\
 s_n^{a,asc} \Delta t_1 & s_e^{a,asc} \Delta t_1 & 0 & 0 & 0 & 0 & 0 & 0 \\
 0 & 0 & 0 & 0 & s_n^{a,asc} \Delta t_2 & s_e^{a,asc} \Delta t_2 & 0 & 0 \\
 s_n^{a,dsc} \Delta t_1 & s_e^{a,dsc} \Delta t_1 & 0 & 0 & 0 & 0 & 0 & 0 \\
 0 & 0 & 0 & 0 & s_n^{a,dsc} \Delta t_2 & s_e^{a,dsc} \Delta t_2 & 0 & 0 \\
 \frac{\partial h}{\partial x_n} & \frac{\partial h}{\partial x_n} & -1 & 0 & 0 & 0 & 0 & 0 \\
 0 & 0 & 0 & 0 & \frac{\partial h}{\partial x_n} & \frac{\partial h}{\partial x_n} & -1 & 0
 \end{bmatrix} = \begin{bmatrix} v_1^n \\ v_1^e \\ v_1^{u1} \\ v_1^{u2} \\ v_2^n \\ v_2^e \\ v_2^{u1} \\ v_2^{u2} \end{bmatrix} = \begin{bmatrix} \rho_1^{r,asc} \\ \rho_2^{r,asc} \\ \rho_1^{r,dsc} \\ \rho_2^{r,dsc} \\ \rho_1^{a,asc} \\ \rho_2^{a,asc} \\ \rho_1^{a,dsc} \\ \rho_2^{a,dsc} \\ 0 \\ 0 \end{bmatrix}. \quad (13)$$

Note that in this context, 4D refers to the four variables found during the inversion: v^n , v^e , v^{u1} , and v^{u2} with $v^u = v^{u1} + v^{u2}$. This problem offers the most informative solution but only when splitting vertical deformation into SPF and non-SPF components is justifiable, such as in the case of glacier flow.

Since the processing time of large datasets can be very long and hence to avoid having to reprocess the same dataset, MSBAS always generates both deformation time series d_i and deformation rate (flow velocity) time series v_i

3. Implementation

The MSBAS Software is written in C++ and is designed to run under the Linux operating system. It can likely be adapted to run under other operating systems, but this was not tested. When it is run on workstations, MSBAS uses OpenMP to distribute processing between the available CPU cores. The maximum number of CPU cores accessible by MSBAS is controlled by the *OMP_NUM_THREADS* environment variable. When it is run on clusters, MSBAS uses MPI to distribute processing between the allocated nodes, and then, on each node, MSBAS uses OpenMP to distribute processing between the available CPU cores.

3.1. Dependencies

The MSBAS Software uses the Standard Template Library (STL) and Exception Handling. MSBAS is linked to the LAPACK library, which provides the *DGELSD* subroutine for matrix operations, and to the Geospatial Data Abstraction Library (GDAL) for reading and writing raster files. The two makefiles, provided with the software, can be used for compiling MSBAS on for two environments, either workstations or clusters. Supplementary files, aspect angle and topographic derivatives can be computed using the GDAL *gdaldem* program and Generic Mapping Tools (GMT) *grdmath* and *grdgradient* programs.

3.2. Input parameter file

MSBAS accepts one input parameter, which is the processing parameter file name. This file contains processing control flags and specifies the datasets to be processed. Processing control flags are described below.

3.3. Input dataset file(s)

A dataset is a collection of deformation products, such as DInSAR, SPO-RO, or SPO-AO, acquired with identical acquisition parameters, such as satellite azimuth and SAR incidence angle. SPO-RO and SPO-AO must have separate dataset files.

Table 3. Mandatory (bold font) and optional MSBAS processing control flags.

Parameter	Type	Value(s)	Description
FORMAT	<i>i</i>	0	4 bytes float small-endian format
	<i>i</i>	1	4 bytes float big-endian format
	<i>i, i</i>	2, Δr <i>x, y</i>	GeoTiff format, Δr try [0–3] columns, rows, e.g., 1000, 1000 pixels
FILE_SIZE	<i>i, i</i>		
WINDOW_SIZE	<i>i, i, i, i</i>	x_a, x_b, y_a, y_b	default: 0, x_1 , 0, y_1
C_FLAG	<i>i</i>	0	default: no calibration
	<i>i, ..., i</i>	[1–9], $x_1, y_1, x_2, y_2, \dots, \Delta x, \Delta y$	1–9 reference region(s), Δx and Δy try [0–32]
	<i>i</i>	10	zero average
	<i>i, i, i</i>	100, $\Delta x, \Delta y$	minimal Z-score, Δx and Δy try [0–32]
R_FLAG	<i>i</i>	0	default: no regularization
L_FLAG	<i>i, f</i>	[1, 2, 3], λ	zeroth (1), first (2) or second (3) order regularization, λ try [0.01–0.1]
	<i>i</i>	0	default: MSBAS-1D/2D/3D depending on data
	<i>i, s, s, i</i>	$1, \frac{\partial h}{\partial x_n}, \frac{\partial h}{\partial x_e}, 3$	MSBAS-3DSPF (requires R_FLAG = 1, λ)
SPA	<i>i, s</i>	$1, \frac{\partial h}{\partial x_n}, \frac{\partial h}{\partial x_e}, 4$	MSBAS-4D
	<i>i</i>	2, α_h	MSBAS-3DAPF (requires R_FLAG = 1, λ)
	<i>f</i>	0	default: temporal sampling base on data
	<i>i</i>	[0.0–1.0]	samples per year, e.g., 0.2 – one sample per five years (i.e., 1/0.2=5)
TREND	<i>i</i>	[1–N]	samples per year, e.g., 1 – one sample per year
	<i>i</i>	0	default: do not subtract trend
PLEVEL	<i>i</i>	1	MSBAS-1D only, subtract and then add trend (requires R_FLAG = 1, λ)
SEASON	<i>i</i>	2	default: compute SVD for each line and for each partially coherent pixel
	<i>i</i>	0	compute stack only for each set
	<i>i</i>	1	MSBAS-1D only, compute SVD for each line only
SET	<i>f, f</i>	0.0, 1.0	default: use all data
	<i>i, s, f, f, s</i>	[0.0–1.0], [0.0–1.0]	start and stop fraction of year, e.g., 0.3,0.7 or 0.8,0.2 e.g., 0, 122435, -189, 34, set.txt (DInSAR/SPO-RO – 0, SPO-AO – 1)
#	<i>i, s, f, s, s, s</i>	[0,1], $hhmmss, \theta, \phi, set, lv_theta, lv_phi$	e.g., 0, 122435, -189, 34, set.txt, lv_theta.tif, lv_phi.tif
			comment

Types are *i* – integer, *f* – float and *s* – string. Square brackets indicate that only one value is permitted (e.g., [0, 1] – either 0 or 1, [0.0–1.0] – one number in range 0.0–1.0). Δr is interpolation radius. *x* and *y* are width and length of interferograms. x_a, x_b, y_a and y_b are first and last columns and rows of sub-region to be processed. x_i and y_i are column number and row number of reference region(s), up to nine regions are supported. Δx and Δy are half-width/length of reference region(s). λ is regularization parameter. $\frac{\partial h}{\partial x_n}, \frac{\partial h}{\partial x_e}$ are files with first derivatives of elevation along north and east directions. α_h is file with elevation aspect angle measured in radians. In SET, first parameter indicates DInSAR or SPO-RO (0) or SPO-AO (1) data. *hhmmss* is set's acquisition time (must be six digits). θ and ϕ are satellite azimuth and SAR incidence angle, measured in degrees. *lv_theta* and *lv_phi* are files with look vector elevation and orientation angles at each map pixel. Lines can be commented with # symbol.

The dataset file lists the deformation products of a specific dataset. It describes a path to a file, a perpendicular baseline in meters, and acquisition dates in the YYYYMMDD format of primary and secondary images. The perpendicular baseline values are no longer used and can be set to any arbitrary value; they are left there for compatibility with previous versions of the software.

3.4. Input data

Input data consist of the deformation products, stored as raster files, geocoded to the same grid, and converted to meters or other displacement units (e.g., mm, cm). Overall output products have the same displacement units as input data, but time is always measured in years. In the case of MSBAS-1D,

deformation products can remain in satellite coordinates and radians if desired; in that case, the output products are also in radians and radians/year.

DInSAR and RO products are of a positive sign when the deformation is toward the satellite (i.e., apparent uplift), and AO products are of a positive sign when the deformation is in the direction of the satellite heading (i.e., northern deformation is positive in the ascending data).

All raster files (deformation products and some supplementary files) must be in the same raster format and resampled to the same geographic grid. While many raster formats are supported by GDAL, the GeoTiff format with NAN values set to zero was tested the most and, therefore, is recommended. Raster files from different datasets can be resampled

to the same geographic grid with the GDAL *gdalwarp* command and *te* and *tr* or *ts* flags.

3.5. Processing control flags

Several control flags control the processing flow of MSBAS (Table 3). If a control flag consists of a string with more than one parameter, successive parameters are separated by a comma. The *FORMAT* control flag controls the format of the input data: four bytes float small-ending (value 0), four bytes float big-endian (1), and GDAL-supported (usually GeoTiff) raster formats (2) are permitted. In the latter case, it is possible to fill missing values (i.e., incoherent pixels masked out during unwrapping) by interpolation, using the GDAL's *GDALFillNodata* subroutine and a search window Δr . The typical values of Δr range from 0 to 5 pixels; a value of 0 disables the interpolation, and values from 1 to 3 pixels are recommended.

FILE_SIZE specifies the number of columns and rows in raster files. The optional *WINDOW_SIZE* selects a region within the data set for processing. This helps to reduce memory requirements and execution time when the processing of the entire area is not required. However, instead of using the *WINDOW_SIZE*, it is recommended to crop raster files externally, for example, with GDAL's *gdalwarp* command.

Deformation products contain measurements relative to an arbitrarily chosen reference region. The calibration step ensures that, prior to processing, all deformation products are consistently referenced to one or more common reference regions. *C_FLAG* controls the way each deformation product is calibrated. The most common approach is to use a single reference region (value = 1), but up to nine reference regions (value = 1 to 9) of the same size are supported. It is also possible to disable the calibration (value = 0, if deformation products are calibrated externally), to set the average value of each deformation product to zero (value = 10), or to select the statistically best-fit reference point where the value of the Z-score for the entire set is minimal (value = 100). In the latter case, the half-window values Δx in x (columns) and Δy in y (rows) directions are tested, and if they cannot be accommodated due to the lack of coherent pixels, their values are reduced by one until the Z-score is calculated. The recommended values of *C_FLAG* are 100 (best choice, unless the location of the reference region is known a priori), 1, and 10.

R_FLAG controls an order of the regularization (none, zeroth, first, second) and a value of the regularization parameter λ . The recommended value of *R_FLAG* is 2 (first order regularization) and of λ in the range 0.01 to 0.1.

The optional control flag *L_FLAG* makes it possible to specify the SPF (1) or APF (2) constraint. In the case of the SPF constraint, if azimuth offsets are also provided, setting the last parameter to 3 starts 3DSPF processing and 4 starts 4D processing.

The optional parameter *SPA* (samples per annum) controls the resampling of time series to a coarser resolution in the time domain. For example, a value of 1 means one sample per year, and a value of 0.5 means one sample every two years (i.e., $1/0.5=2$). The starting time is always aligned with the time of the first SAR acquisition.

The optional parameter *TREND* is only valid for 1D analysis. If this parameter is set to 1, then a mean deformation rate (trend) is computed using the stacking technique and subtracted from the data (detrending). Then, the regular MSBAS-1D processing is performed on detrended data, and then, the mean rate previously computed with stacking is added. It is recommended to use $R_FLAG=1,\lambda$ during this scenario. This type of processing is used in regions covered by snow for part of a year, resulting in gaps in temporal data coverage and a disconnected network. Without detrending, the most used $R_FLAG=2,\lambda$ causes incorrect interpolation across temporal gaps (e.g., winters), and $R_FLAG=1,\lambda$ underestimates the deformation trend. By detrending data first, this type of processing correctly captures the overall trend and its inter-annual variability, if no significantly different deformation occurs during the temporal gap with no data.

The optional parameter *SEASONAL* makes it possible to select data during a specified season each year and neglect other data. For example, *SEASONAL*=0.246,0.831 results in selecting deformation products that fall into the March 31 to October 31 period each year, which is approximately a snow-free season in Canada. *SEASONAL*=0.831,0.246 results in selecting deformation products that fall into the October 31 to next-year March 31 period.

The optional parameter *PLEVEL* is only applicable for 1D analysis. When set to 0, the software quickly computes the deformation rate by stacking and then exits. When set to 1, the software calculates the deformation rate for pixels that are coherent in all interferograms. In this case, the SVD

Table 4. Satellite data used in studies.

Region	Technique	Data	Span	ϕ°	θ°	nSLC	nInSAR
NWT, Canada	1D seasonal/trend	Sentinel-1 166-202 (asc) Google Earth base layer Sentinel-1 077-1201 (asc)	20170416–20231030 extracted 20240426	341	39	104	258
Colombia	1D, 2D	Sentinel-1 171-0572 (dsc) Sentinel-2	20160321–20211214	348	40	112	166
Argentina	2D	Sentinel-1 018-1029 (asc) Sentinel-1 141-0744 (dsc) Sentinel-2	20161121–20221105 20161121–20221105 20230228	346 195	39 39	153 142	252 197
Turkey	2D	Sentinel-1 043-119/124 (asc) Sentinel-1 123-461/466 (dsc) Sentinel-2	20170606–20230130 20170606–20230130 20220919	347 193	40 40	160 161	436 437
Yemen	2D	Sentinel-1 043-042 (asc) Sentinel-1 108-542 (dsc) Sentinel-2	20150217–20210621 20150217–20210621 20230120	348 192	40 40	154 136	145 675
NWT, Canada	2D, 3DSPF, 3DAPF	Sentinel-1 079-221 IW3-1,2 (asc) Sentinel-1 108-221 IW1-4,5 (asc) Sentinel-1 116-366 IW1-3,4 (dsc) Sentinel-2	20161020–20221007 20170319–20220329 20161020–20221007 20210621	338 338 202 33	43 33 33	147 128 164	246 262 262
Alaska	3D, 4D	Sentinel-1 050-192 (asc) Sentinel-1 116-391 (dsc) Sentinel-2	20170303–20240419 20170217–20240411 20230604	342 198	40 40	141 205	140 204

ϕ is the satellite azimuth and θ is the SAR incidence angle, nSLC and nInSAR are the numbers of available images and interferograms produced.

inversion is computed only once for the entire interferogram line, which may be slower than in the previous case. When set to 2, the software computes deformation rates for all the pixels that are coherent in at least some interferograms. In this case, SVD inversion is computed for each pixel of the interferogram separately, which may be slow. *SET* defines each input dataset. The first parameter specifies whether it is a DInSAR/SPO-RO (0) or SPO-AO (1) dataset. Other parameters are the acquisition time (*hhmmss*), ϕ and θ , the satellite azimuth and SAR incidence angles measured in degrees, and the name of a dataset file. If the dataset consists of data obtained only on ascending passes or only on descending passes, then the 1D algorithm is applied, which ignores satellite azimuth and SAR incidence angles, but they still need to be specified to preserve formatting. It is possible to provide two additional files with look vector elevation angle Θ and orientation angle Φ at each map pixel for computing precise directional cosines. These files can be produced with the GAMMA *look_vector* command.

3.6. Output products

The output of the MSBAS Software consists of two sets of raster files: instantaneous deformation rate (flow velocity) time series for each acquisition epoch, typically used for studying glacier flow, and cumulative deformation time series for each acquisition epoch, used for other studies. File dimensions and units are those provided in the input data files. The

linear deformation rate, standard deviation, and coefficient of determination are also computed by applying linear regression. In the case of non-linear deformation, however, the linear deformation rate can be misleading. The coefficient matrix is stored in a text file; it can be used, for example, for rank and singular value analysis. Solution and residual norms are also stored in separate raster files. All screen output is stored in a text log file. The rank values for each pixel are stored in a raster rank file. This file can be used in postprocessing for masking out low-rank pixels.

3.7. Limitations and future work

The behavior of the software was tested with several thousand datasets worldwide (see citations in Table 2 and Samsonov and Feng 2022). During these tests, the software performed very well and failed only when there was a problem with the hardware. However, sometimes, the behavior of the software was suboptimal. Two such scenarios are described below.

When run on a cluster, MSBAS distributes an equal number of raster lines to each processing node. Sometimes, some raster lines have a small number of pixels, for example, when the part of a study area is over water and is masked out. These lines are processed rapidly, but processing lines with many pixels takes longer. As a result, all nodes are held up until all lines are processed on all nodes. In future versions, it would be desirable to distribute processing to different nodes based on an equal number of valid pixels rather than an equal number of lines. It is, however,

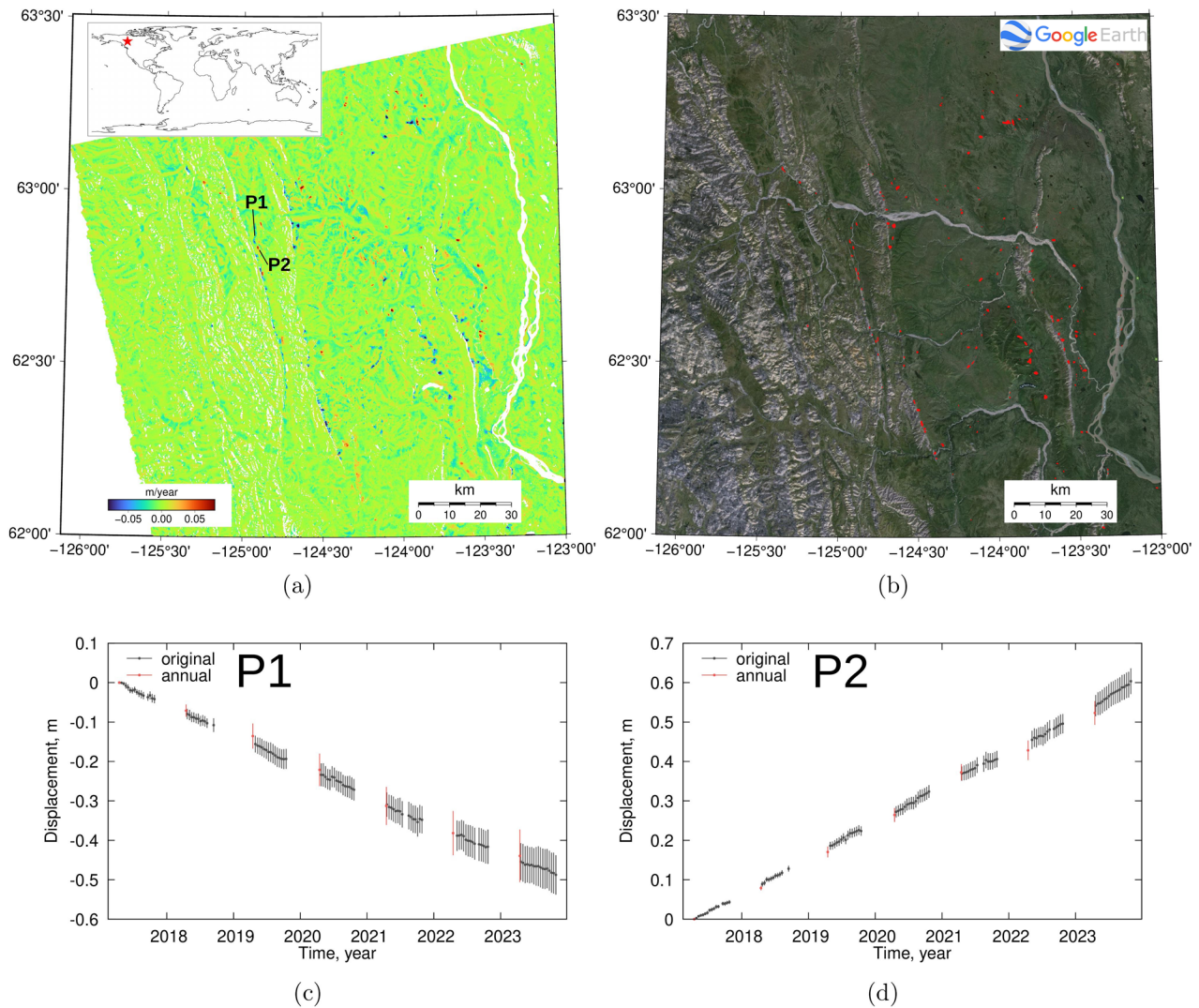


Figure 1. Results of MSBAS-1D processing of Sentinel-1 data obtained on ascending passes during snow-free seasons for area in Northwest Territories (NWT), Canada : (a) 2017–2023 line-of-sight (LOS) deformation rate, eastward/downward deformation is negative and westward/upward is positive; (b) areas with fast deformation rates that are likely slow-moving landslides are indicated on optical image extracted from Google Earth; (c–d) original (in black) and annual (in red) deformation time series at P1 and P2. Contains modified Copernicus Sentinel data [2017–2023].

challenging because the number of coherent pixels in each line is apriori unknown and is computed during the processing.

MSBAS uses C++’s *calloc* subroutine to allocate virtual memory. The software becomes slow when an operating system uses swap memory instead of RAM. The amount of required memory is computed and provided in a log file. It is recommended to reduce the size of a study area or the number of supplied deformation products or to increase RAM to avoid using swap memory.

An overarching issue is that the quality of output deformation products depends on the quality of the input data. Beyond the computational aspects, the main objective of the follow-up research remains the development of the methodology for identifying

properly unwrapped pixels. Presently, pixels are selected based on their coherence. If the coherence threshold value is too high, many properly unwrapped pixels are lost, reducing the overall spatial coverage, but if it is too low, noise is introduced, reducing overall measurement precision. This, however, is an objective of interferometric processing research and is beyond the scope of this study.

4. Results

Table 4 lists the Sentinel-1 Single-Look Complex (SLC) datasets used to create the deformation products in this study. The SLC datasets were processed with GAMMA software (Wegmüller et al. 2016) to produce either interferograms or range/azimuth offset

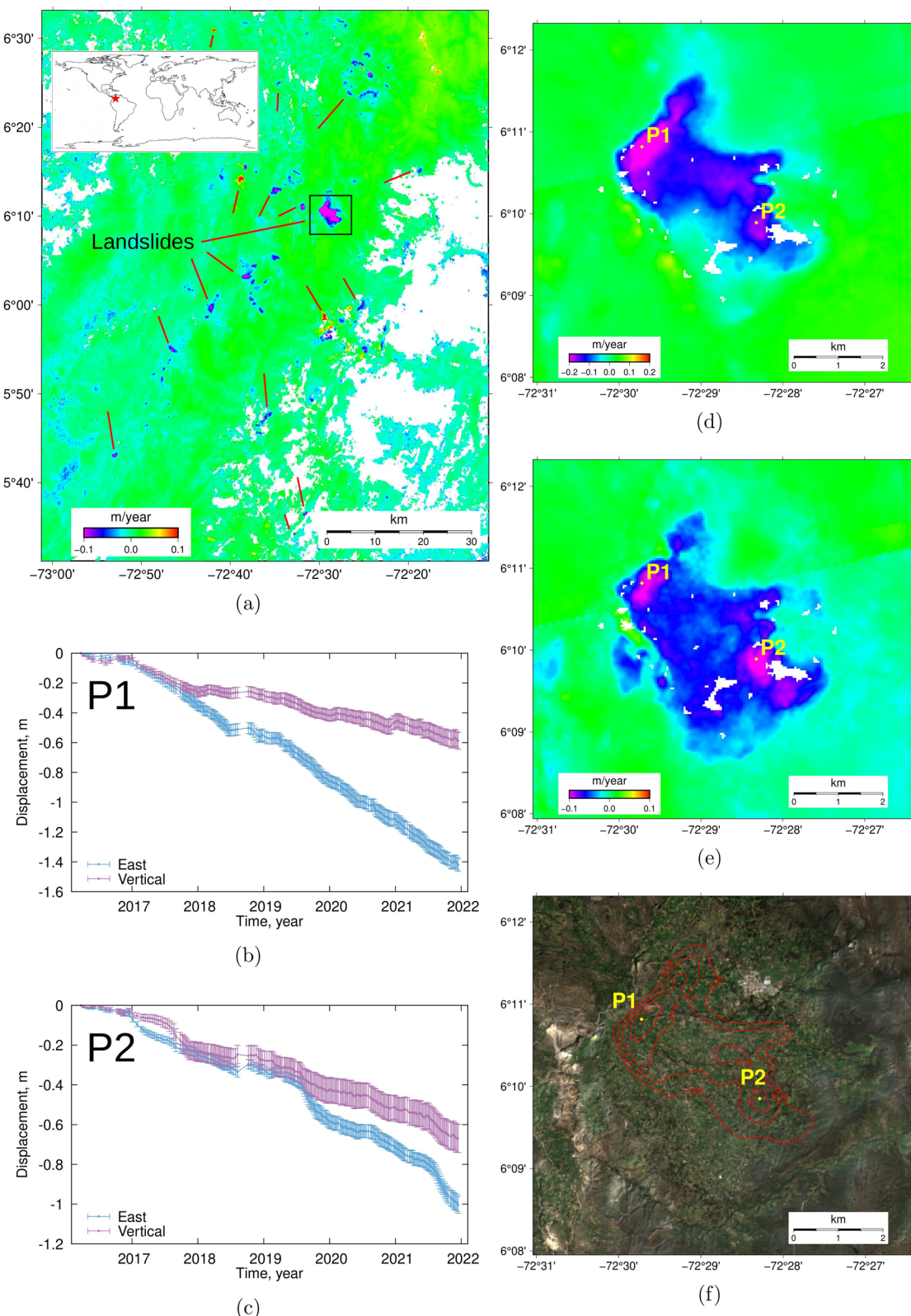


Figure 2. Results of MSBAS-1D/2D processing of Sentinel-1 data obtained on ascending and descending passes for area in Colombia: (a) 2016–2021 line-of-sight (LOS) deformation rate on descending pass, westward/downward deformation is negative and eastward/upward is positive, several landslides are marked with red lines; (b–c) time series of ground deformation at P1 and P2; (d–e) horizontal east and vertical deformation rates computed for subset outlined in black in (a); (f) contour lines of horizontal east rate from (d), in range 0.05–0.20 m/year, are indicated on Sentinel-2 image. Contains modified Copernicus Sentinel data [2016–2021].

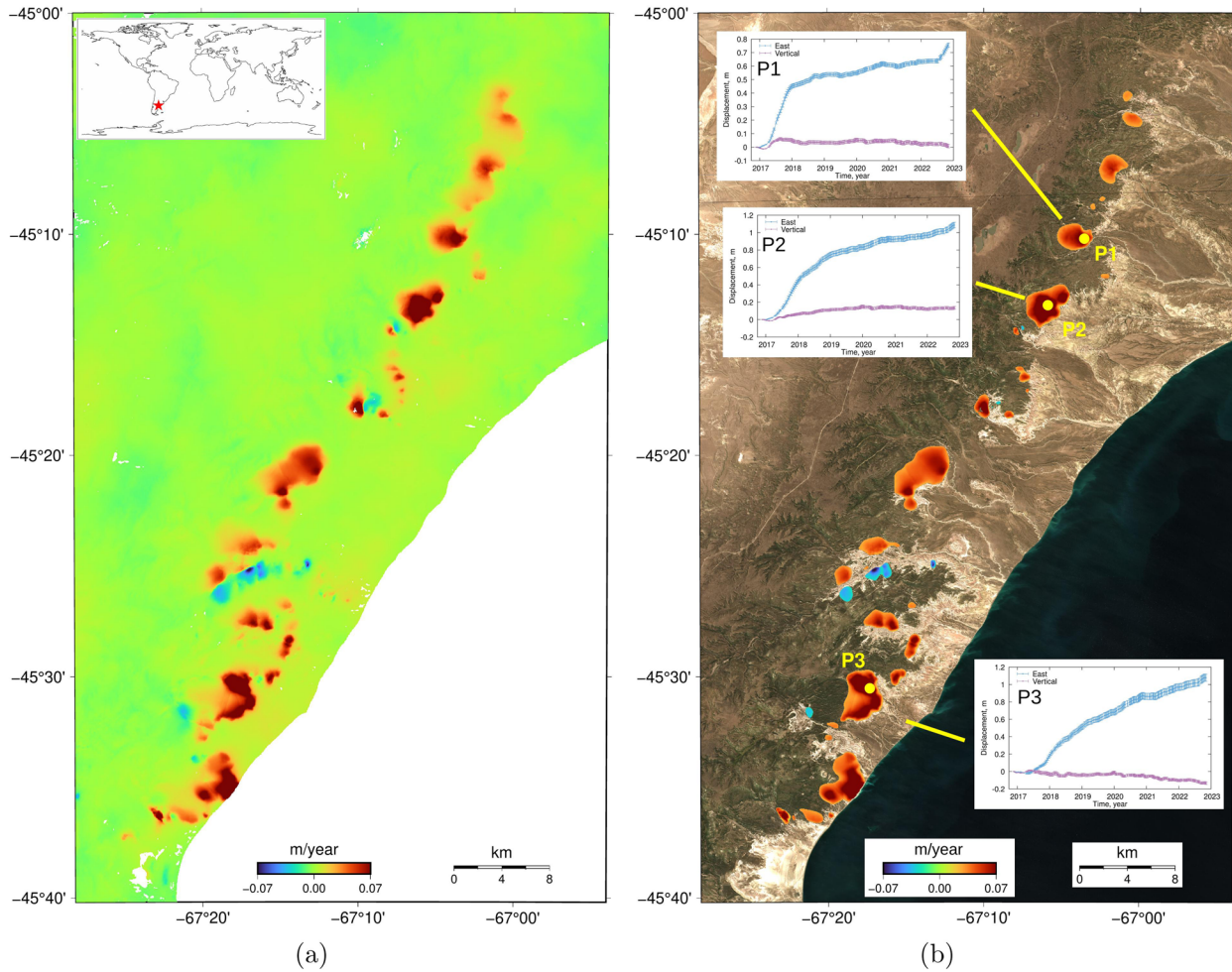


Figure 3. Results of MSBAS-2D processing of Sentinel-1 data obtained on ascending and descending passes for area in Argentina: (a) 2016–2022 horizontal east deformation rate, westward deformation is negative and eastward is positive; (b) areas with fast deformation rates that are likely slow-moving deep-seated landslides are indicated on Sentinel-2 image, inserts show 2D deformation time series at P1, P2, and P3. Contains modified Copernicus Sentinel data [2016–2023].

products, and then deformation time series were computed with MSBAS Software. Sentinel-2 and Google Earth data were utilized as a base layer to indicate the locations of the actively deforming regions.

Figure 1 shows an area in the Northwest Territories (NWT), Canada, where the line-of-sight deformation rate was calculated using 2017–2023 Sentinel-1 data obtained on ascending passes during snow-free seasons. The MSBAS-1D technique with the *TREND*=1 parameter was used for this calculation (Figure 1a). In the figure, eastward and downward deformation is represented by negative values, while westward and upward deformation is represented by positive values. The areas exhibiting deformation rates greater than 0.08 m/year, which indicate slow-moving, deep-seated landslides, were identified and plotted as red polygons overlaid on the optical image (Figure 1b).

The original time series at sites P1 and P2 are shown in black, and the annual deformation time series computed with the *SPA*=1 parameter (i.e., one sample per year) are shown in red (Figure 1c,d). The computation time required to produce such time series on a standard workstation is short.

Figure 2 shows an area in Colombia, where the line-of-sight deformation rate was calculated from 2016 to 2021 Sentinel-1 data obtained on descending passes using the MSBAS-1D technique (Figure 2a). In the figure, westward and downward deformation is represented by negative values, while eastward and upward deformation is represented by positive values. Several slow-moving, deep-seated landslides were observed and marked with red lines. The MSBAS-2D technique was then applied to a subset (black rectangle in Figure 2a) of Sentinel-1 data obtained on ascending and descending passes where the largest landslide was observed. The

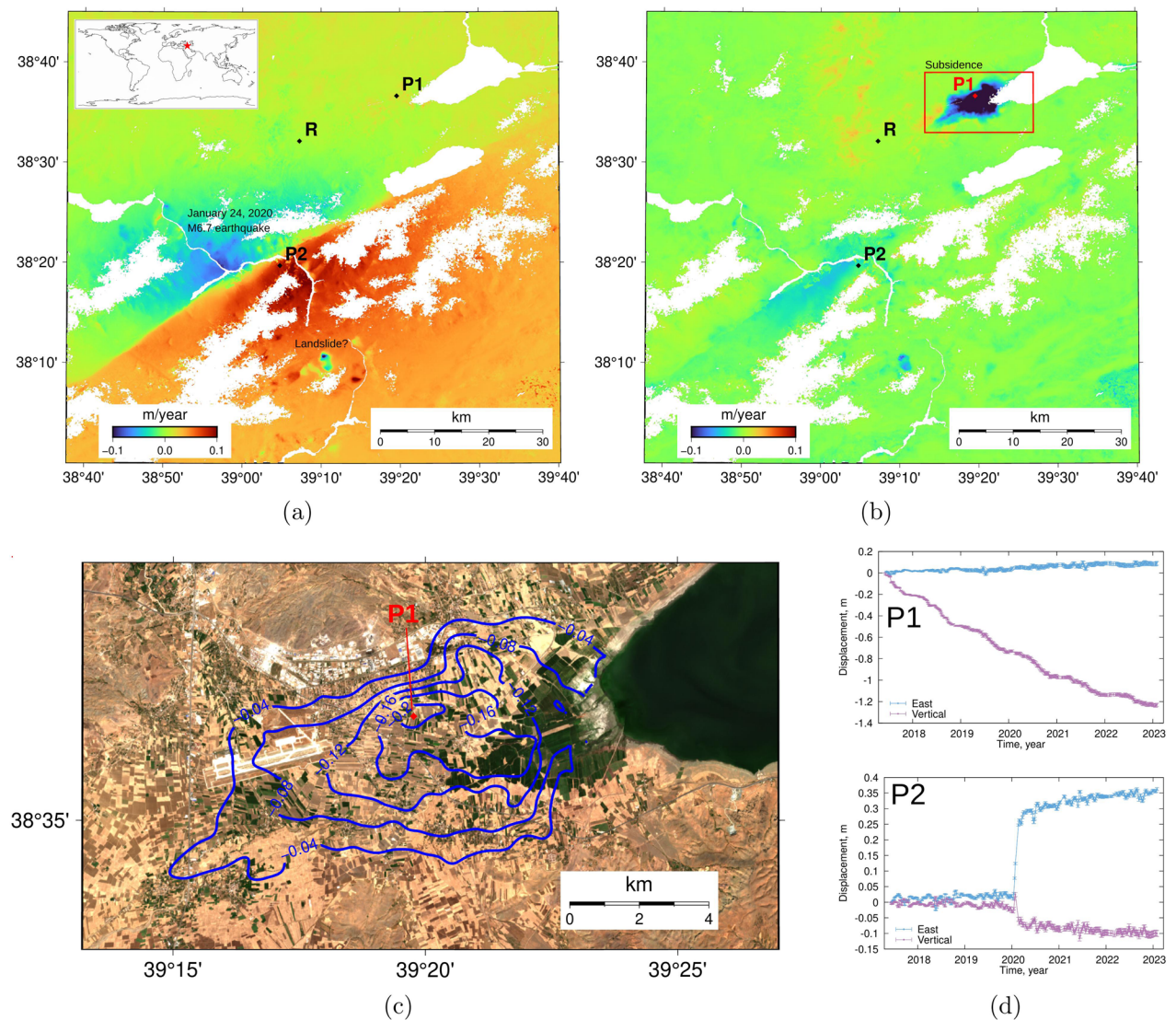


Figure 4. Results of MSBAS-2D processing of Sentinel-1 data obtained on ascending and descending passes for area in Turkey: (a–b) 2017–2023 horizontal east and vertical deformation rates computed relative reference region R, westward/downward deformation is negative and eastward/upward is positive; (c) area experiencing rapid subsidence with contour lines of subsidence rate from (b), in range 0.04–0.20 m/year, indicated on Sentinel-2 image; (d–e) time series of ground deformation at P1 and P2, observed horizontal deformation is due to January 24, 2020, M6.7 earthquake and landslide, observed vertical deformation is likely due to extraction of groundwater. Contains modified Copernicus Sentinel data [2017–2023].

resulting 2D east and vertical time series at sites P1 and P2 are shown in Figure 2b,c and the east and vertical deformation rates in Figure 2d,e. Contour lines of the east deformation rate (ranging from 0.05 to 0.20 m/year) are indicated on the Sentinel-2 image in Figure 2f.

Figure 3 shows an area in Argentina, where the east deformation rate was computed from 2016 to 2022 Sentinel-1 data obtained on ascending and descending passes using the MSBAS-2D technique (Figure 3a). In this figure, westward deformation is represented by negative values, while eastward by positive values. Areas with fast deformation rates

that are likely slow-moving landslides were identified, and the extent of the landslides was indicated on the Sentinel-2 image (Figure 3b). Inserts show the 2D deformation time series at sites P1, P2, and P3.

Figure 4 shows an area in Turkey, where various deformation processes were observed in the region northeast of the epicenter of the 2023 Kahramanmaraş earthquake sequence. The east and vertical deformation rates were computed from 2017 to 2023 Sentinel-1 data obtained on ascending and descending passes using the MSBAS-2D technique relative to the reference region R. Figure 4a,b illustrate these rates. An

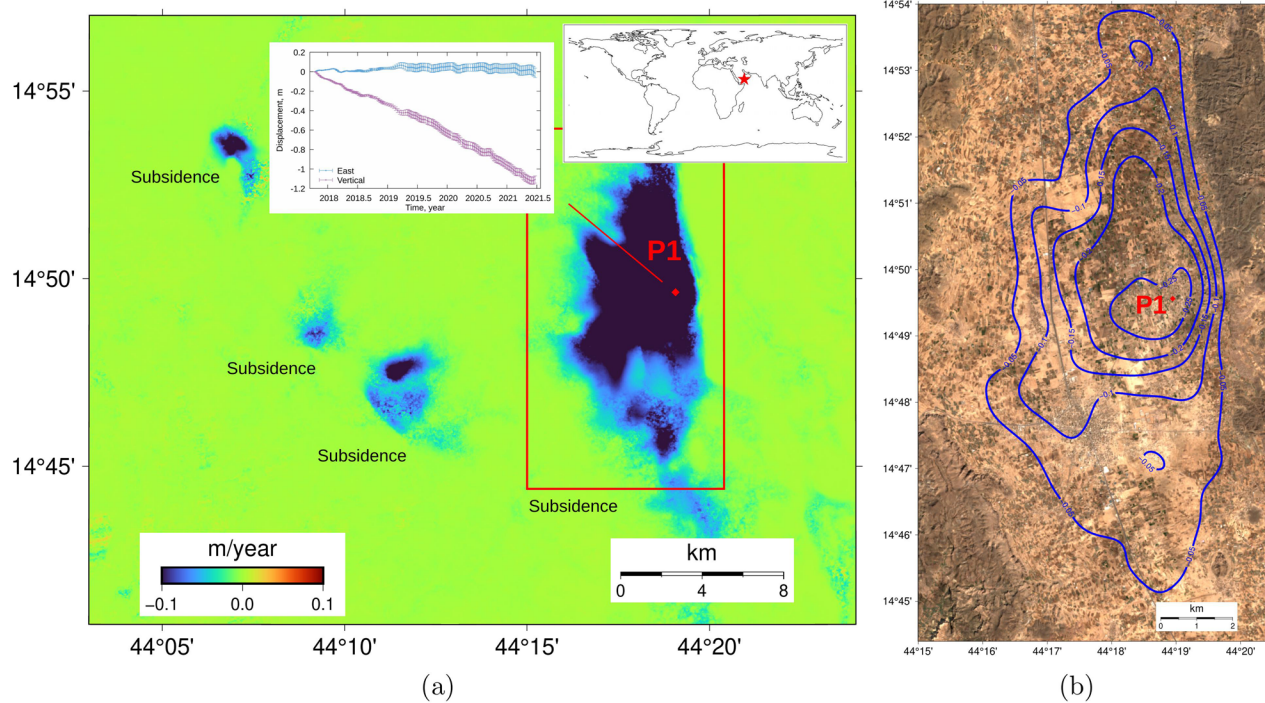


Figure 5. Results of MSBAS-2D processing of Sentinel-1 data obtained on ascending and descending passes for area in Yemen: (a) 2015–2021 vertical deformation rate, subsidence is negative, insert shows deformation time series at P1; (b) area experiencing rapid subsidence with contour lines of subsidence rate from (a), in range 0.05–0.25 m/year, indicated on Sentinel-2 image. Contains modified Copernicus Sentinel data [2015–2023].

area experiencing rapid subsidence is shown with contour lines of subsidence in the 0.04–0.20 m/year range indicated on the Sentinel-2 image in Figure 4c. Furthermore, Figure 4d shows the time series of ground deformation at sites P1 (top) and P2 (bottom). The observed horizontal deformation is due to the 24 January 2020 M6.7 Elazig earthquake (i.e., post-seismic deformation) and landslides. The observed vertical deformation is likely caused by the extraction of groundwater.

Figure 5 shows an area in Yemen, where ground subsidence was observed around the town of Mabar. The vertical deformation rate computed from 2015 to 2021 Sentinel-1 data obtained on ascending and descending passes using the MSBAS-2D technique is shown in Figure 5a. An insert in the figure shows the deformation time series at site P1. Figure 5b shows an area experiencing rapid subsidence with contour lines of subsidence rate in the 0.05–0.25 m/year range indicated on the Sentinel-2 image. The subsidence is likely caused by the extraction of groundwater.

The results of the constrained inversion of the Sentinel-1 data obtained on ascending and descending passes for an area in the Northwest Territories, Canada, where a large slow-moving deep-seated landslide was previously observed and discussed in detail in Samsonov and Blais-Stevens (2024) are shown in Figure 6. The

landslide boundary (in red) indicated on the Sentinel-2 image is displayed in Figure 6a. The results of MSBAS-2D processing are presented in Figure 6b, showing the 2017–2022 vertical deformation rate represented as a color-coded image, and the east deformation rate represented as vectors and contour lines ranging from 0.10 (dark red) to 0.44 (purple) m/year. The 2D deformation time series at P1 and P2 are shown in Figure 6c. Furthermore, the results of MSBAS-3DSPF processing are illustrated in Figure 6d–f, including topographic gradients in the north and east directions, color-coded vertical deformation rate, and horizontal deformation shown as vectors. The results of MSBAS-3DAPF processing are also shown in Figure 6g,h, which display topographic aspect angle measured from north clockwise, color-coded vertical deformation rate and horizontal deformation shown as vectors.

The results of MSBAS-3D/4D processing for the Malaspina Glacier in southeastern Alaska are shown in Figure 7. Figure 7a displays the 2017–2024 magnitude of 3D/4D flow velocity, with the central flow line and 10 km marks plotted in green and blue. Figure 7b shows the time series of the magnitude of 3D/4D flow velocity extracted along the central flow line. A glacier surge was observed during 2020–2021 in the bottom 40 km of the glacier. Additionally, Figure 7c,d present the time series of cumulative flow

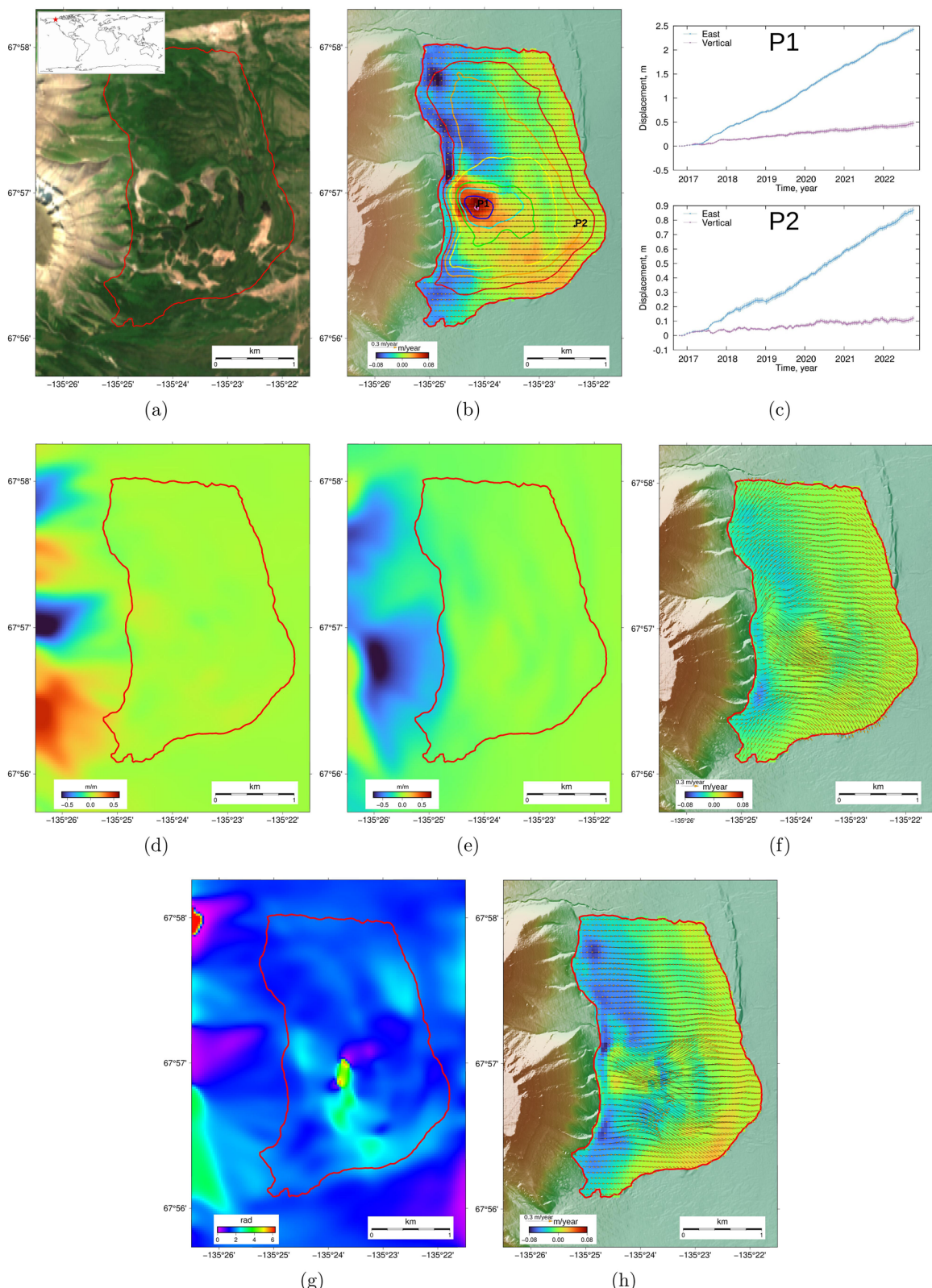


Figure 6. Results of MSBAS-2D/3DSPF/3DAPF processing of Sentinel-1 data obtained on ascending and descending passes for area in Northwest Territories, Canada: (a) Sentinel-2 image and landslide boundary (in red); (b) 2D results, 2017–2022 vertical deformation rate is color-coded and horizontal east deformation is shown as vectors and contour lines in range 0.10 (dark red) – 0.44 (purple) m/year; (c) deformation time series at P1 and P2; (d–e) topographic gradients in north and east directions; (f) 3DSPF results, vertical deformation rate is color-coded and horizontal east deformation is shown as vectors; (g) topographic aspect angle, measured from north clockwise; (h) 3DAPF results, vertical deformation rate is color-coded and horizontal east deformation is shown as vectors. Contains modified Copernicus Sentinel data [2017–2022].

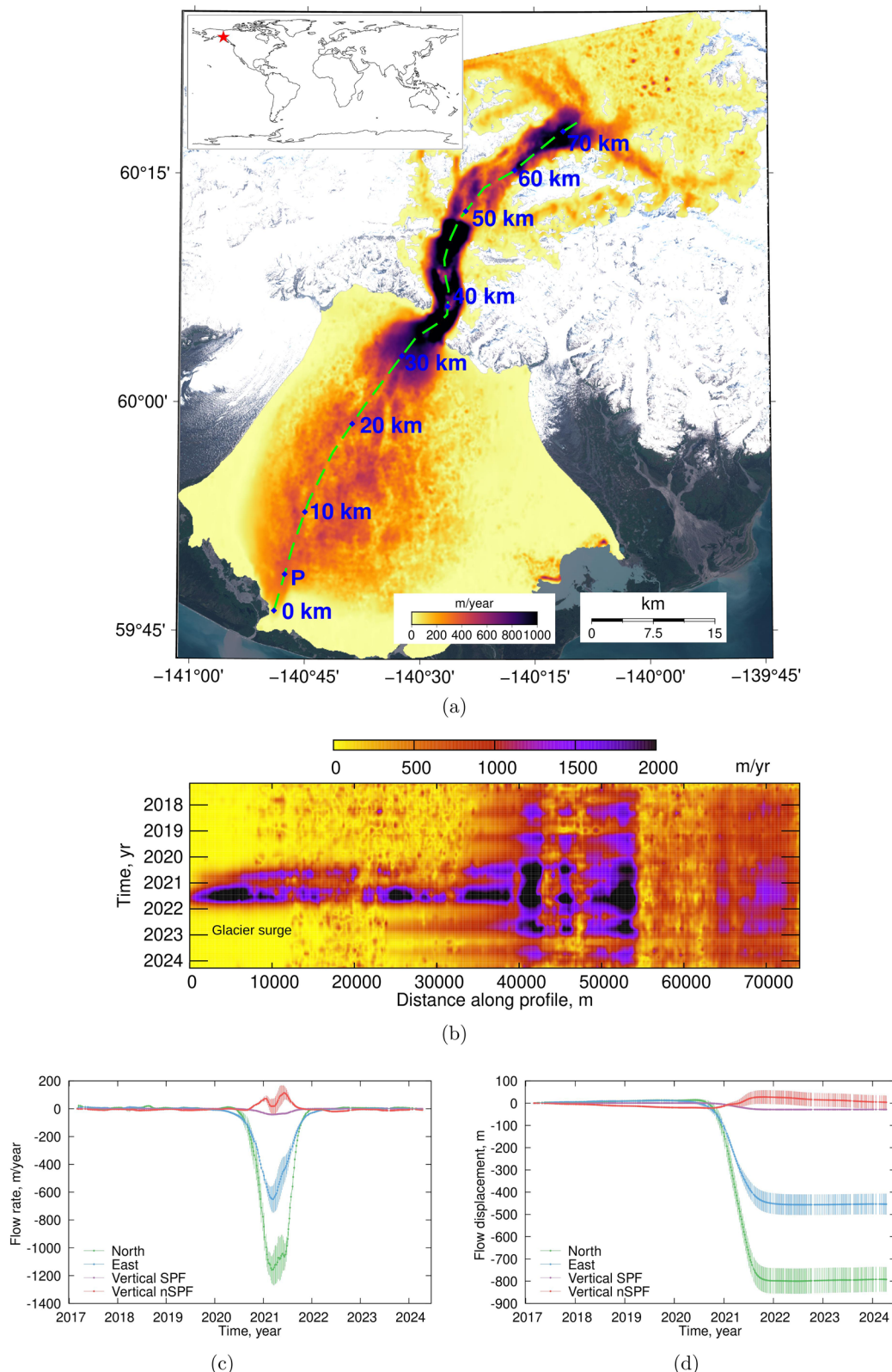


Figure 7. Results of MSBAS-3D/4D processing of Sentinel-1 data obtained on ascending and descending passes for area in south-eastern Alaska: (a) 2017–2024 magnitude of 3D/4D flow velocity, central flowline and 10km marks are plotted in green and blue; (b) time series of magnitude of 3D/4D flow velocity along central flow line, glacier surge is observed during 2020–2021; (c-d) time series of flow rates and flow displacements at P. Contains modified Copernicus Sentinel data [2017–2024].

displacements and flow rates at P, affected by the 2020–2021 surge. A detailed explanation of the MSBAS-3D technique can be found in Samsonov et al. (2021a) and the MSBAS-4D technique in Samsonov et al. (2021b).

5. Conclusions

This study has illustrated the new functionality of the MSBAS Software Version 10 through analysis of active deformation processes in seven diverse settings from around the world. Six examples have revealed new findings, while the seventh, located in the Northwest Territories, Canada, has been previously described (Samsonov and Blais-Stevens 2024). The theoretical framework for the technique is found in Samsonov and d’Oreye (2012, 2017); Samsonov et al. (2021a) is not elaborated, but the governing equations for the 1D–4D cases are explicitly presented for reference.

MSBAS Software Version 10 is designed to run on workstations and clusters and to produce time series from partially coherent data. As the processing time of large datasets is quite long, MSBAS outputs all the products that may be used to subsequently enhance the results to avoid reprocessing. For example, in postprocessing, pixels with a low rank can be removed using the rank information provided in a raster rank file. As a second example, the time series for specific pixels can be extracted in a text format using *msbas_extract* and plotted with the *msbas_plot_ts.sh* script.

For testing MSBAS 1D and 2D functionality, the preprocessed Sentinel-1 DInSAR data used for computing 2D deformation time series for a large landslide in Colombia, shown in Figure 2b–e, is provided with the source code. These data was produced by an automated processing system (Dudley and Samsonov 2020, 2021) and was not manually quality controlled; thus, it may contain unwrapping errors. For testing MSBAS 3D, 3DSPF, and 4D functionality, additional data for a flooded potash mine can be downloaded from Samsonov (2020a), and for several North-American glaciers from Samsonov (2020b, 2021).

This manuscript is intended as a comprehensive MSBAS Version 10 Software Manual. The MSBAS Software Version 10 can be downloaded from Samsonov (2024). Future MSBAS enhancements will be logged and described in Samsonov (2024).

Acknowledgements

Sentinel-1 data were acquired by the European Space Agency and distributed by the National Aeronautics and Space Administration and Alaska Satellite Facility. Sentinel-2 data were acquired by the European Space Agency and distributed by the Copernicus Service. One image was extracted from Google Earth Pro. Figures were plotted with GMT 6.0.0 and Gnuplot 5.2 software. NRCan contribution number/Numéro de contribution de RNCan: 20230005. The author extends his deepest gratitude to George Choma of the Canada Centre for Remote Sensing, NRCan, and the CJRS Associate Editor for assisting in proofreading. The MSBAS Software Version 10 and test data can be downloaded from Samsonov (2024).

Disclosure statement

No potential conflict of interest was reported by the author(s).

References

- Camacho, A.G., Fernández, J., Samsonov, S.V., Tiampo, K.F., and Palano, M. 2020. “3D multi-source model of elastic volcanic ground deformation.” *Earth and Planetary Science Letters*, Vol. 547: pp. 116445. doi:[10.1016/j.epsl.2020.116445](https://doi.org/10.1016/j.epsl.2020.116445).
- Czarnogorska, M., Samsonov, S., and White, D. 2016. “Airborne and spaceborne remote sensing characterization for Aquistore carbon capture and storage site.” *Canadian Journal Remote Sensors*, Vol. 42 (No. 3): pp. 274–290. doi:[10.1080/07038992.2016.1171131](https://doi.org/10.1080/07038992.2016.1171131).
- d’Oreye, N., Derauw, D., Samsonov, S., Jaspard, M., and Smittarello, D. 2021. MaSTer: A full automatic multi-satellite InSAR mass processing tool for rapid incremental 2D ground deformation time series. Paper presented at 2021 IEEE International Geoscience and Remote Sensing Symposium, Brussels, Belgium, July 2021. doi:[10.1109/igarss47720.2021.9553615](https://doi.org/10.1109/igarss47720.2021.9553615).
- Derauw, D., d’Oreye, N., Jaspard, M., Caselli, A., and Samsonov, S. 2020. “Ongoing automated ground deformation monitoring of Domuyo - Laguna del Maule area (Argentina) using Sentinel-1 MSBAS time series: Methodology description and first observations for the period 2015–2020.” *Journal of South American Earth Sciences*, Vol. 104: pp. 102850. doi:[10.1016/j.jsames.2020.102850](https://doi.org/10.1016/j.jsames.2020.102850).
- Dille, A., Dewitte, O., Handwerger, A.L., d’Oreye, N., Derauw, D., Bamulezi, G.G., Mawe, G.I., et al. 2022. “Acceleration of a large deep-seated tropical landslide due to urbanization feedbacks.” *Nature Geoscience*, Vol. 15 (No. 12): pp. 1048–1055. doi:[10.1038/s41561-022-01073-3](https://doi.org/10.1038/s41561-022-01073-3).
- Dille, A., Kervyn, F., Handwerger, A.L., d’Oreye, N., Derauw, D., Mugaruka Bibentyo, T., Samsonov, S., Malet, J.-P., Kervyn, M., and Dewitte, O. 2021. “When image correlation is needed: Unravelling the complex dynamics of a slow-moving landslide in the tropics with dense radar

- and optical time series.” *Remote Sensing of Environment*, Vol. 258: pp. 112402. doi:[10.1016/j.rse.2021.112402](https://doi.org/10.1016/j.rse.2021.112402).
- Dudley, J., and Samsonov, S. 2020. “The Government of Canada automated processing system for change detection and ground deformation analysis from RADARSAT-2 and RADARSAT Constellation Mission Synthetic Aperture Radar data: description and user guide.” Technical Report. Geomatics Canada Open File, No 63.
- Dudley, J., and Samsonov, S. 2021. “Système de traitement automatisé du gouvernement canadien pour la détection des variations et l’analyse des déformations du sol à partir des données de radar à synthèse d’ouverture de RADARSAT-2 et de la mission de la Constellation RADARSAT : description et guide de l’utilisateur.” Technical Report. Geomatics Canada Open File, No 68.
- Lundgren, P., Girona, T., Bato, M.G., Realmuto, V.J., Samsonov, S., Cardona, C., Franco, L., Gurrola, E., and Aivazis, M. 2020. “The dynamics of large silicic systems from satellite remote sensing observations: the intriguing case of Domuyo volcano, Argentina.” *Scientific Reports*, Vol. 10 (No. 1): pp. 11642. doi:[10.1038/s41598-020-67982-8](https://doi.org/10.1038/s41598-020-67982-8).
- Massonnet, D., and Feigl, K. 1998. “Radar interferometry and its application to changes in the Earth’s surface.” *Reviews of Geophysics*, Vol. 36 (No. 4): pp. 441–500. doi:[10.1029/97RG03139](https://doi.org/10.1029/97RG03139).
- Oreye (2012) Samsonov, S., and d’Oreye, N. 2012. “Multidimensional time series analysis of ground deformation from multiple InSAR data sets applied to Virunga Volcanic Province.” *Geophysical Journal International*, Vol. 191 (No. 3): pp. 1095–1108. doi:[10.1111/j.1365-246X.2012.05669.x](https://doi.org/10.1111/j.1365-246X.2012.05669.x).
- Oreye (2017) Samsonov, S.V., and d’Oreye, N. 2017. “Multidimensional Small Baseline Subset (MSBAS) for Two-Dimensional Deformation Analysis: Case Study Mexico City.” *Canadian Journal Remote Sensors*, Vol. 43 (No. 4): pp. 318–329. doi:[10.1080/07038992.2017.1344926](https://doi.org/10.1080/07038992.2017.1344926).
- Pearse, J., Singhroy, V., Samsonov, S., and Li, J. 2014. “Anomalous surface heave induced by enhanced oil recovery in northern Alberta: InSAR observations and numerical modeling.” *Journal of Geophysical Research: Solid Earth*, Vol. 119 (No. 8): pp. 6630–6649. doi:[10.1002/2013JB010885](https://doi.org/10.1002/2013JB010885).
- Rosen, P., Hensley, P., Joughin, I., Li, F., Madsen, S., Rodriguez, E., and Goldstein, R. 2000. “Synthetic aperture radar interferometry.” *Proceedings of the IEEE*, Vol. 88 (No. 3): pp. 333–382. doi:[10.1109/5.838084](https://doi.org/10.1109/5.838084).
- Samsonov, S. 2017. “Short- and long-term ground deformation due to cyclic steam stimulation in Alberta, Canada, measured with interferometric radar.” *The Leading Edge*, Vol. 36 (No. 1): pp. 36–42. doi:[10.1190/tle36010036.1](https://doi.org/10.1190/tle36010036.1).
- Samsonov, S. 2019. “Three-dimensional deformation time series of glacier motion from multiple-aperture DInSAR observation.” *Journal of Geodesy*, Vol. 93 (No. 12): pp. 2651–2660. doi:[10.1007/s00190-019-01325-y](https://doi.org/10.1007/s00190-019-01325-y).
- Samsonov, S. 2020a. “Data for: Estimation of deformation intensity above a flooded potash mine near Berezniki (Perm Krai, Russia) with SAR interferometry.” Mendeley Data Vol. 1. doi:[10.17632/CKC3HGZ2DH.1](https://doi.org/10.17632/CKC3HGZ2DH.1).
- Samsonov, S. 2020b. “Data for: SAR-derived flow velocity and its link to glacier surface elevation change and mass balance.” Mendeley Data Vol. 1. doi:[10.17632/9D96C5BDDM.1](https://doi.org/10.17632/9D96C5BDDM.1).
- Samsonov, S. 2021. “Data for: Measuring the state and temporal evolution of glaciers in Alaska and Yukon using SAR-derived 3D time series of glacier surface flow.” Mendeley Data Vol. 1. doi:[10.17632/ZF67RSGYDV.1](https://doi.org/10.17632/ZF67RSGYDV.1).
- Samsonov, S. 2024. “Source code of the *Multidimensional Small Baseline Subset (MSBAS) Software Version 10 for multidimensional constrained and unconstrained deformation analysis of partially coherent DInSAR and speckle offset data*.” Technical Report. Geomatics Canada Open File, (No 80). doi: [10.4095/pbcc4f9bv3](https://doi.org/10.4095/pbcc4f9bv3).
- Samsonov, S., and Baryakh, A. 2020. “Estimation of deformation intensity above a flooded potash mine near Berezniki (Perm Krai, Russia) with SAR interferometry.” *Remote Sensing*, Vol. 12 (No. 19): pp. 3215. doi:[10.3390/rs12193215](https://doi.org/10.3390/rs12193215).
- Samsonov, S., and Blais-Stevens, A. 2023. “Satellite interferometry for regional assessment of landslide hazard to pipelines in north eastern British Columbia, Canada.” *International Journal of Applied Earth Observation and Geoinformation*, Vol. 118 pp. 103273. doi:[10.1016/j.jag.2023.103273](https://doi.org/10.1016/j.jag.2023.103273).
- Samsonov, S., and Feng, W. 2022. “Preliminary retrievals of deformation rates based on 2017–2023 Sentinel-1 data computed with the MSBAS system.” Mendeley Data, Vol. 3. doi: [10.17632/t7wvtrk28y.3](https://doi.org/10.17632/t7wvtrk28y.3).
- Samsonov, S., Czarnogorska, M., and White, D. 2015. “Satellite interferometry for high-precision detection of ground deformation at a carbon dioxide storage site.” *International Journal of Greenhouse Gas Control*, Vol. 42 pp. 188–199. doi:[10.1016/j.ijggc.2015.07.034](https://doi.org/10.1016/j.ijggc.2015.07.034).
- Samsonov, S., d’Oreye, N., and Smets, B. 2013a. “Ground deformation associated with post-mining activity at the French-German border revealed by novel InSAR time series method.” *International Journal of Applied Earth Observation and Geoinformation*, Vol. 23 pp. 142–154. doi:[10.1016/j.jag.2012.12.008](https://doi.org/10.1016/j.jag.2012.12.008).
- Samsonov, S., Dille, A., Dewitte, O., Kervyn, F., and d’Oreye, N. 2020. “Satellite interferometry for mapping surface deformation time series in one, two and three dimensions: A new method illustrated on a slow-moving landslide.” *Engineering Geology*, Vol. 266 pp. 105471. doi:[10.1016/j.enggeo.2019.105471](https://doi.org/10.1016/j.enggeo.2019.105471).
- Samsonov, S., Feng, W., Peltier, P., Geirsson, H., d’Oreye, N., and Tiampo, K. 2016a. “Multidimensional small baseline subset (MSBAS) for volcano monitoring in two dimensions: opportunities and challenges. Case study Piton de la Fournaise volcano.” *Journal of Volcanology and Geothermal Research*, Vol. 344 pp. 121–138. doi:[10.1016/j.jvolgeores.2017.04.017](https://doi.org/10.1016/j.jvolgeores.2017.04.017).
- Samsonov, S., Gonzalez, P.J., Tiampo, K., and d’Oreye, N. 2013b. “Methodology for spatio-temporal analysis of ground deformation occurring near Rice Lake (Saskatchewan) observed by RADARSAT-2 DInSAR during 2008–2011.” *Canadian Journal Remote Sensors*, Vol. 39 (No. 1): pp. 27–33. doi:[10.5589/m13-005](https://doi.org/10.5589/m13-005).
- Samsonov, S., Tiampo, K., and Cassotto, R. 2021a. “Measuring the state and temporal evolution of glaciers in Alaska and Yukon using synthetic-aperture-radar-derived (SAR-derived) 3D time series of glacier surface flow.” *The Cryosphere*, Vol. 15 (No. 9): pp. 4221–4239. doi:[10.5194/tc-15-4221-2021](https://doi.org/10.5194/tc-15-4221-2021).

- Samsonov, S., Tiampo, K., and Cassotto, R. 2021b. "SAR-derived flow velocity and its link to glacier surface elevation change and mass balance." *Remote Sensing of Environment*, Vol. 258 pp. 112343. doi:[10.1016/j.rse.2021.112343](https://doi.org/10.1016/j.rse.2021.112343).
- Samsonov, S., Tiampo, K., and Feng, W. 2016b. "Fast subsidence in downtown of Seattle observed with satellite radar." *Remote Sensing Applications*, Vol. 4 pp. 179–187. doi:[10.1016/j.rsase.2016.10.001](https://doi.org/10.1016/j.rsase.2016.10.001).
- Samsonov, S.V. 2022. "Operational processing of big satellite data for monitoring glacier dynamics: Case study of Muldrow Glacier." *Remote Sensing*, Vol. 14 (No. 11): pp. 2679. doi:[10.3390/rs14112679](https://doi.org/10.3390/rs14112679).
- Samsonov, S.V., and Blais-Stevens, A. 2024. "Estimating volume of large slow-moving deep-seated landslides in northern Canada from DInSAR derived 2D and constrained 3D deformation rates." *Remote Sensing of Environment*, Vol. 305 pp. 114049. doi:[10.1016/j.rse.2024.114049](https://doi.org/10.1016/j.rse.2024.114049).
- Samsonov, S.V., d'Oreye, N., González, P.J., Tiampo, K.F., Ertolahti, L., and Clague, J.J. 2014a. "Rapidly accelerating subsidence in the Greater Vancouver region from two decades of ERS-ENVISAT-RADARSAT-2 DInSAR measurements." *Remote Sensing of Environment*, Vol. 143 pp. 180–191. doi:[10.1016/j.rse.2013.12.017](https://doi.org/10.1016/j.rse.2013.12.017).
- Samsonov, S.V., Feng, W., and Fialko, Y. 2017. "Subsidence at Cerro Prieto Geothermal Field and postseismic slip along the Indiviso fault from 2011 to 2016 RADARSAT-2 DInSAR time series analysis." *Geophysical Research Letters*, Vol. 44 (No. 6): pp. 2716–2724. doi:[10.1002/2017GL072690](https://doi.org/10.1002/2017GL072690).
- Samsonov, S.V., Feng, W., Blais-Stevens, A., and Eaton, D.W. 2024. "Ground deformation due to natural resource extraction in the Western Canada Sedimentary Basin." *Remote Sensing Applications*, Vol. 34 pp. 101159. doi:[10.1016/j.rsase.2024.101159](https://doi.org/10.1016/j.rsase.2024.101159).
- Samsonov, S.V., González, P.J., Tiampo, K.F., and d'Oreye, N. 2014b. "Modeling of fast ground subsidence observed in southern Saskatchewan (Canada) during 2008–2011." *Natural Hazards and Earth System Sciences*, Vol. 14 (No. 2): pp. 247–257. doi:[10.5194/nhess-14-247-2014](https://doi.org/10.5194/nhess-14-247-2014).
- Samsonov, S.V., Lantz, T.C., Kokelj, S.V., and Zhang, Y. 2016c. "Growth of a young pingo in the Canadian Arctic observed by RADARSAT-2 interferometric satellite radar." *The Cryosphere*, Vol. 10 (No. 2): pp. 799–810. doi:[10.5194/tc-10-799-2016](https://doi.org/10.5194/tc-10-799-2016).
- Samsonov, S.V., Tiampo, K.F., Camacho, A.G., Fernández, J., and González, P.J. 2014c. "Spatiotemporal analysis and interpretation of 1993–2013 ground deformation at Campi Flegrei, Italy, observed by advanced DInSAR." *Geophysical Research Letters*, Vol. 41 (No. 17): pp. 6101–6108. doi:[10.1002/2014GL060595](https://doi.org/10.1002/2014GL060595).
- Samsonov, S.V., Trishchenko, A.P., Tiampo, K., González, P.J., Zhang, Y., and Fernández, J. 2014d. "Removal of systematic seasonal atmospheric signal from interferometric synthetic aperture radar ground deformation time series." *Geophysical Research Letters*, Vol. 41 (No. 17): pp. 6123–6130. doi:[10.1002/2014GL061307](https://doi.org/10.1002/2014GL061307).
- Smittarello, D., d'Oreye, N., Jaspard, M., Derauw, D., and Samsonov, S. 2022. "Pair selection optimization for InSAR time series processing." *Journal of Geophysical Research*, Vol. 127 (No. 3): e2021JB022825. doi:[10.1029/2021JB022825](https://doi.org/10.1029/2021JB022825).
- Strozzi, T., Luckman, A., Murray, T., Wegmüller, U., and Werner, C. 2002. "Glacier motion estimation using SAR offset-tracking procedures." *IEEE Transactions on Geoscience and Remote Sensing*, Vol. 40 (No. 11): pp. 2384–2391. doi:[10.1109/TGRS.2002.805079](https://doi.org/10.1109/TGRS.2002.805079).
- Vasco, D., Samsonov, S.V., Wang, K., Burgmann, R., Jeanne, P., Foxall, W., and Zhang, Y. 2021. "Monitoring natural gas storage using synthetic aperture radar: are the residuals informative?" *Geophysical Journal International*, Vol. 228 (No. 2): pp. 1438–1456. doi:[10.1093/gji/ggab409](https://doi.org/10.1093/gji/ggab409).
- Vasco, D.W., Dixon, T.H., Ferretti, A., and Samsonov, S.V. 2020a. "Monitoring the fate of injected CO₂ using geodetic techniques." *The Leading Edge*, Vol. 39 (No. 1): pp. 29–37. doi:[10.1190/tle39010029.1](https://doi.org/10.1190/tle39010029.1).
- Vasco, D.W., Rutqvist, J., Jeanne, P., Samsonov, S.V., and Hartline, C. 2020b. "Using geodetic data in geothermal areas." *The Leading Edge*, Vol. 39 (No. 12): pp. 883–892. doi:[10.1190/tle39120883.1](https://doi.org/10.1190/tle39120883.1).
- Wegmüller, U., Werner, C., Strozzi, T., Wiesmann, A., Frey, O., and Santoro, M. 2016. "Sentinel-1 support in the GAMMA software." *Procedia Computer Science*, Vol. 100 pp. 1305–1312. doi:[10.1016/j.procs.2016.09.246](https://doi.org/10.1016/j.procs.2016.09.246).